Biogeochemical implication of massive episodic flood deposition: Model-Data integration

Stanley Nmor[1,✉], Eric Viollier[1], Lucie Pastor[2], Bruno Lansard[1], and Christophe Rabouille[1,✉]

[1] Laboratoire des Sciences du Climat et de l'Environnement, LSCE/IPSL,CEA-CNRS-UVSQ-Université Paris Saclay, 91198 Gif sur Yvette, France

[2] ABF Décisions

Corresponding author: Stanley Nmor (stanley.nmor@lsce.ipsl.fr), Christophe Rabouille (christophe.rabouille@lsce.ipsl.fr)

Key Points:

- The study focuses on two different flood depositions (thick organic-poor and thin organic-rich), with distinct biogeochemical responses
- Highlights the role of internal storage of DIC for organic-poor vs near surface effluxes of carbon across the SWI and enhanced metal cycling
- Demonstrates the possibility of flood-induced memory effect on carbon mineralization pathway with pronounced impact on methanogenesis

Abstract

Coastal deltas are depocenter for materials transported from riverine channels. Under regime of extreme flood events, this zone can experience large sediment deposition within a short period. However, the biogeochemical consequences of such disturbances on the carbon and other element cycles are not fully understood. Using a coupled data-model approach, we explore the early diagenesis responses of coastal sediment influenced by two intense flood discharges (in spring and fall) by the Rhône river in 2008. The data set shows that biogeochemical fluxes and rates responded abruptly to this almost instantaneous change in sediment deposition. These flood-related depositions increased organic carbon mineralization by a factor of 2 to 6 compared to pre-flood levels, previously dominated by sulfate reduction (72%), and methanogenesis (8%). The two floods represented (organic-poor in spring and organic-rich in fall) cause different responses of the diagenetic system in terms of dissolved inorganic carbon (DIC) fluxes - the organic-poor flood deposition induced a large storage of DIC in porewaters, whereas the organic-rich induced a large efflux of DIC along the entire relaxation. The model reveals that intense redox cycling and mineral precipitation were responsible for the non-euxinic (sulfide-free) sediment after flood deposition. The sequential flood depositions reveal a temporary memory effect (i.e. an interaction between two successive floods), with stronger effect for methane (44%), whose relatively long relaxation timescale limits complete recovery before the

next event 6 months after the first one. Increasing frequency and intensity of these events could lead to memory accumulation of flood biogeochemical signature.

Plain Language Summary

Coastal sediments are subject to episode of intense flood deposition which can triggers biogeochemical changes in the sediment. However, our understanding of the response and magnitude of the changes induced by these events is still poorly known. Here, we use a numerical model of early diagenesis and dataset from two floods in 2008 driven by discharges from the Rhône river to investigate the size and scope of the biogeochemical dynamics following these events. Our findings suggest that these floods could cause differing biogeochemical responses, the extent of which is determined by the underlying characteristics of the flood layer deposit. Using the model, we found a 2-6 times increase in overall bacterial recycling rates from pre-flood condition which resulted to different response of dissolved inorganic carbon (DIC) flux out of the sediment. Under this condition, significant internal metal recycling and production of sulfide minerals can be enhanced. In the event of sequential flood deposition, cumulative biogeochemical changes or “memory effect of flood deposition” can also occur which affect the recovery of sediment after the flood. These effects might be more consequential if these intense floods continue to increase.

1. Introduction

River-dominated ocean margins (RiOMar) are important for connecting the terrestrial and marine organic carbon cycles (OC) (Mackenzie et al., 2004; Regnier et al., 2022) by filtering the transfer of material from the River systems on continent margins to the open ocean. They also serve as a major organic matter (OM) deposition center, which has implications for preservation and burial. Indeed, continental margins account for more than 85 % of all organic carbon burial in the ocean, with deltas (RiOMars) representing half of the shelf burial (Burdige, 2005). At the same time, river deltas are active biogeochemical reactors that emit large quantities of CO_2 to the atmosphere (Cai, 2011; Dai et al., 2022).

These RiOMar systems are also vulnerable to extreme flood events, which are known to transport large amounts of sediment, carbon and nutrients from the land to the oceans, with their primary depositional zone occurring preferentially in the connecting deltas (McKee et al., 2004). Massive sediment inputs driven by these flood events have been observed in many of such systems: for example, Amazon River (Aller et al., 1996; Montanher et al., 2018),

Mississippi River (Morse and Rowe, 1999), Atchafalaya River (Allison et al., 2000), Eel River (Bentley and Nittrouer, 2003), Po River (Palinkas et al., 2005; Tesi et al., 2012; Tesi et al., 2013), Têt River (Bourrin et al., 2008), Rhône River (Cathalot et al., 2010). These large and nearly instantaneous transfers of sediment are projected to occur with increasing frequency due to changing environmental landscapes and climate change (Tockner and Stanford, 2002). Indeed, the current trend in extreme precipitation from hurricanes and other storm events can result in large amounts of sediment being delivered in a short period of time, as documented in some coastal margins: Tropical Storm Lee transported sediment to a large portion of Cheapeake Bay via the Susquehanna River (Cheng et al., 2013), extreme precipitation events in the Mississippi River basin transferred a large volume of terrestrial organic carbon to the northern Gulf of Mexico (Bianucci et al., 2018), large volumes of sediment were transported on the Northeastern Australian coast during Cyclone Winifred (Carter et al., 2009), to name a few. All of these events have been shown to have a short (daily)-to-medium (yearly) impact on the ecosystem productivity, such as degrading water clarity and growth of phytoplankton (Cheng et al., 2013), increasing mineralization in bottom waters of the coastal ocean inducing hypoxic condition (Cheng et al., 2013; Moriarty et al., 2021), or increased CO_2 flux to the atmosphere (Osburn et al., 2019).

In the Gulf of Lions (the southern part of France), about 80% of the annual terrigenous particulate input is delivered by Rhône river floods (Antonelli et al., 2008) with a large majority of the materials deposited in the prodeltaic zone (Ulses et al., 2008). The sediment delivered by these flood events can differ in terms of its quantity and quality, as they represent a conglomeration of different particles originating from different regions of the catchment (Eyrolle et al., 2012; Pont et al., 2017). In addition, given the unique sedimentary characteristics of the prodelta (high sedimentation up to 40 $cm\ yr^{-1}$, high carbon flux up to 650 $gC\ m^{-2}yr^{-1}$), the underlying diagenetic sequence of sediment shows remarkable stationarity during spring and summer (high concentration of DIC, dissolved iron and manganese, strong sulfate reduction Rassmann et al. (2020)) despite short-term biogeochemical response linked to fall and winter floods (Cathalot et al., 2010). The reason for such long-term stability but short-term response is still unknown (Pastor et al., 2018), but has been linked to a rather short system's relaxation timescale (4-5 months) and the existence of a possible "*Biogeochemical attractor*" - a hypothetical concept basically associated with the rapid reorganisation of the perturbed porewater profiles to their pre-flood condition despite being affected by such massive depositional event (Nmor et al., 2022). The latter would help explain the maintenance of the same diagenetic characteristic for multi-temporal data in non-steady conditions (Nmor et al.,

2022). While a proper understanding of the characteristics of this type of perturbation requires continuous monitoring and observation in both long- and short-term basis (Ferreira et al., 2023; Toussaint et al., 2014), there is still a scarcity of data on the estimated biogeochemical fluxes and rates caused by these flood events. Combination of available data (Bonifácio et al., 2014; Bourgeois et al., 2011; Cathalot et al., 2010; Pastor et al., 2018), with appropriate spatio-temporal scale, and numerical modelling can thus help to answer some of these questions.

This study aims to quantify the size and scope of biogeochemical changes brought about by significant flood events in the Rhône prodelta region. A reactive transport model with a non-steady state approach was used to investigate how the diagenetic mineralization of organic matter can explain porewater data obtained from observations of two distinct flood deposition events in 2008. We also calculated the biogeochemical fluxes and rates associated with these events, as well as the system's temporal evolution after this perturbation. The effect of this phenomenon on carbon, iron, manganese, and sulfur cycling was then determined. The results of this model-data investigation give new insights on the consequences of these extreme events on sediment biogeochemical dynamics.

2. Materials and Methods

2.1 Data description

The dataset discussed in this paper entails the flood driven deposition events which occurred in the Rhône prodelta in the year 2008 (Cathalot et al., 2010; Pastor et al., 2018). The data described the hydro-sedimentological and chemical situation of the sediment in the proximal station within 2 km from the river mouth (Station A: 4°51.099 °E and 43°18.751 °N). The average depth at this location is 23 m (Pastor et al., 2018) with high apparent accumulation rates up to 40 $cm\ yr^{-1}$ (Charmasson et al., 1998).

Our concern in this work is the flood events of May/June 2008 (Generalized flood) and November/December 2008 (Cenevol flood) (Pastor et al., 2018). These two floods have been dubbed the spring and fall floods, respectively. The sampling dates are specified in Fig. 1. In the spring flood, 30 cm of sediment was deposited. The average organic carbon content in this layer of sediment (1% d.w.) was lower than the average OC in pre-flood sediment (> 2% d.w.); Cathalot et al. (2010)), with deposited materials primarily composed of aggregated siliceous and carbonate crystalline rocks from nearby tributaries (Durance and Isère rivers) containing large amounts of refractory carbon (Cathalot et al., 2013; Copard et al., 2018). During the fall flood, a sediment layer of 10 cm thickness was deposited mostly composed of silicate minerals and

organic debris with a high OC content sediment containing large amounts of young OC (5% d.w.; Cathalot et al. (2010)). Porewater composition including dissolved iron (Fe^{2+}) and manganese (Mn^{2+}) profiles in both events showed evidence of this flood perturbation, with these species responding sequentially to the deposition (Pastor et al., 2018). This response was characterized by a slow build-up of iron following manganese release in the first 30 cm of porewater. Furthermore, significant sulfate reduction was observed within the sediment, with sulfide concentrations below the detection limit. Full description of the dataset can be found in Cathalot et al. (2010) and Pastor et al. (2018).

2.2 Model description

The model used for this study is the time dependent, one dimensional reactive transport model, FESDIA (Nmor et al., 2022). This model described the transformation of OC within the sediment column with well adapted capabilities for usage in sudden flood depositional scenarios. The full description of the model can be found in Nmor et al. (2022) and detailed mass balance equations and reaction kinetic is provided in the Appendix. Here, we basically recap the key biogeochemical reactions and pathway necessary to simulate the flood datasets derived from Pastor et al. (2018).

The reactive transport model includes 16 state variables: fast (C_{org}^{fast}) and slow C_{org}^{slow} degradable organic matter, two pools of manganese oxide (MnO_{2A} and MnO_{2B}) and iron hydroxide ($FeOOH_A$ and $FeOOH_B$), manganese carbonate ($MnCO_3$) all constitute the particulate solid modeled (Table 1). The choice of iron and manganese fractions was dictated by the assumption that the short-term path of Fe and Mn dynamics is driven by the reactive pool of their respective oxides. In practice, iron oxide pool broadly consists of highly reactive (amorphous and crystalline) oxides - ferrihydrite, goethite, lepidocrocite and hematite) with half-life of < 1 yr (Canfield et al., 1992; Raiswell and Canfield, 1998), moderately reactive component (magnetite and reactive silicate of half-life of 10^2 yr), poorly reactive iron oxide with longer half-life, > 10^5 yr (Canfield et al., 1992; Poulton et al., 2004). Detrital iron fraction bound within sheet silicates are nonreactive on the timescale of early diagenetic processes of concern to the model (Poulton and Raiswell, 2002) while particulate iron bound to sulfide (FeS and FeS_2) when formed via precipitation have high stability and low solubility, thus can be permanently buried (see below and Rassmann et al. (2020)). As such, these solid phases of iron are not modeled. Similarly, manganese oxides or (oxyhydroxides) in the sediment span different reactive timescales and only the reactive fractions are considered in the model. Our modeling strategy is analogous to other diagenetic

models that describe metal cycling in marine sediment (Berg et al., 2003; Dale et al., 2015; Zhao et al., 2020).

Dissolved species included in the model are oxygen (O_2), nitrate (NO_3), ammonium (NH_4^+), dissolved iron (Fe^{2+}) and manganese (Mn^{2+}), sulfate (SO_4^{2-}), hydrogen sulfide (H_2S), methane (CH_4) and dissolved inorganic carbon (DIC) (Table 1).

Table 1: State variables described in the model.

State variable	Description	Model notation	Units
C_{org}^{fast}	Fast decaying detritus	FDET	$mmol\ C\ m^{-3}$
C_{org}^{slow}	Slow decaying detritus	SDET	$mmol\ C\ m^{-3}$
$FeOOH_A$	Fast oxidized ferric iron	FeOOHA	$mmol\ Fe\ m^{-3}$
$FeOOH_B$	Slow oxidized ferric iron	FeOOHB	$mmol\ Fe\ m^{-3}$
MnO_{2A}	Fast oxidized manganese	MnO2A	$mmol\ Mn\ m^{-3}$
MnO_{2B}	Slow oxidized mangenese	MnO2B	$mmol\ Mn\ m^{-3}$
O_2	Oxygen	O2	$mmol\ O_2\ m^{-3}$
NO_3^-	Nitrate	NO3	$mmol\ N\ m^{-3}$
NH_4^+	Ammonium	NH3	$mmol\ N\ m^{-3}$
SO_4^{2-}	Sulfate	SO4	$mmol\ S\ m^{-3}$
H_2S	Hydrogen sulfide	H2S	$mmol\ S\ m^{-3}$
Fe^{2+}	Reduced ferrous iron	Fe	$mmol\ Fe\ m^{-3}$
Mn^{2+}	Reduced manganese	Mn	$mmol\ Mn\ m^{-3}$
DIC	Dissolved inorganic carbon	DIC	$mmol\ C\ m^{-3}$
CH_4	Methane	CH4	$mmol\ C\ m^{-3}$
$MnCO_3$	Mn carbonate	MnCO3	$mmol\ Mn\ m^{-3}$

Degradation of organic matter (OM) occurs via the sequence of energy utilization of electron acceptors, with oxygen used first, followed by oxidation via NO_3. Thereafter, the model includes microbially mediated reduction by the oxides of Mn and Fe (MnO_2 and $FeOOH_3$) with this justification largely dictated by the substantial release of their respective reduced solutes during flood deposition (Pastor et al., 2018). Sulfate reduction and methanogenesis close the carbon-based cycle of OM remineralization in the model (Eq. 1).

$$
\begin{aligned}
OM + O_2 &\rightarrow CO_2 + \frac{1}{(C:N)} NH_3 + H_2O \\
OM + 0.8NO_3^- + 0.8H^+ &\rightarrow CO_2 + \frac{1}{(C:N)} NH_3 + 0.4N_2 + 1.4H_2O \\
OM + 2MnO_{2A} + 4H^+ &\rightarrow CO_2 + \frac{1}{(C:N)} NH_3 + 2Mn^{2+} + 3H_2O \\
OM + 4FeOOH + 8H^+ &\rightarrow CO_2 + \frac{1}{(C:N)} NH_3 + 4Fe^{2+} + 7H_2O \\
OM + 0.5SO_4^{2-} + H^+ &\rightarrow CO_2 + \frac{1}{(C:N)} NH_3 + 0.5H_2S + H_2O \\
OM &\rightarrow 0.5CO_2 + \frac{1}{(C:N)} NH_3 + 0.5CH_4
\end{aligned}
\qquad (1)
$$

where OM is simply represented as $(CH_2O)(NH_3)_{N:C}$) and N:C is the redfield nitrogen to carbon ratio respectively (N:C = $\frac{16}{106}$). The reactive rate is represented by a Michaelis-Menten type relationship with respect to the oxidant concentration (see Appendix).

The direct consequence of organic matter remineralization in the model is the production of reduced substances (Eq. 1). The model considers a series of subsequent processes connected to these reduced species (Eq. 2). In order to reduce the degree of freedom for calibrating poorly constrained parameters and processes which govern many of the secondary reaction in the Rhône prodelta sediment, a simplified representation of the iron, manganese and sulfur interactions was made.

Re-oxidation of reduced species from OM mineralization via oxygen (Eq. 2) and metallic oxides (Eq. 2) is included while methane formed by fermentation of OM can be anaerobically oxidized (i.e anaerobic oxidation of methane, AOM) (Dale et al., 2006). Fe^{2+} is oxidized to ferric iron (Fe^{3+}), which precipitates out as fresh iron oxide ($FeOOH_A$) minerals. Sulfide produced by sulfate reduction is abiotically oxidized by both pools of iron oxyhydroxydes and manganese oxides (i.e sulfur-mediated iron and manganese reduction) (Berg et al., 2003). As discussed in Haese (2000), the interaction between dissolved Fe^{2+} and H_2S happens in two stages, with the formation of intermediate dissolved elemental sulfur (S^0) and dissolved FeS (FeS_{aq}). However, these forms of sulfur are not modeled because of their unstable nature in marine sediment as well as the possibility of FeS_{aq} to precipitate to its particulate form (FeS_p) once a solubility threshold of ~ 2 µM is reached (Rickard, 2006). Therefore, we assumed that dissolved FeS, upon formation, is subsequently transforms into a stable form of particulate sulfur that can be eliminated from the porewaters via precipitation (Rickard, 1997, 2006). The kinetic rate expressions of all re-oxidation processes and other secondary reaction are described by standard second-order rate formulation.

The model also includes a simple representation of the formation and dissolution of Mn carbonates. However, iron carbonate (siderite) formation and dissolution was not considered in the model since siderite precipitation is inhibited by low levels of sulfide (Haese, 2000). This is precisely the situation in the Rhône pro-delta sediment in which FeS precipitation is the dominant sink for dissolved iron and is produced through the sediment column (Rassmann et al., 2020). This kinetics of dissolution and precipitation follow a similar formulation in Wang and Van Cappellen (1996), where the reaction rates are dependent on the pore water saturation state. Here, the pH of the porewater was not explicitly modeled but was fixed at a constant value of 7.5 in order to reduce the complexity of the model (Berg et al., 2003).

$$
\begin{aligned}
NH_4^+ + 2O_2 &\rightarrow NO_3^- + H_2O + 2H^+ \\
2Mn^{2+} + O_2 + 2H_2O &\rightarrow 2MnO_{2A} + 4H^+ \\
4Fe^{2+} + O_2 + 6H_2O &\rightarrow 4FeOOH_A + 8H^+ \\
H_2S + 2O_2 &\rightarrow SO_4^{2-} + 2H^+ \\
CH_4 + 2O_2 &\rightarrow CO_2 + 2H_2O \\
2Fe^{2+} + MnO_{2A/B} + 2H_2O &\rightarrow 2FeOOH_A + Mn^{2+} + 2H^+ \\
H_2S + MnO_{2A/B} + 2H^+ &\rightarrow S^0 + Mn^{2+} + 2H_2O \\
H_2S + 2FeOOH_{A/B} + 4H^+ &\rightarrow S^0 + 2Fe^{2+} + 4H_2O \\
CH_4 + SO_4^{2-} &\rightarrow HCO_3^- + HS^- + H_2O \\
Fe^{2+} + H_2S &\rightarrow FeS + 2H^+ \\
Mn^{2+} + HCO_3^- &\leftrightarrow MnCO_3 + H^+
\end{aligned}
\qquad (2)
$$

2.3 Model Parameters

The key rate parameters for the biogeochemical processes are tabulated in Table 2 . The environmental parameters and boundary conditions were derived from previous steady-state modelling studies investigated in the Rhône prodelta sediment (Ait Ballagh et al., 2021; Pastor et al., 2011b). For our model-data calibration, parameters associated with the transport processes were first adjusted before pathways involving the carbon dynamics were fine-tuned.

The specification of the carbon-based parameters was carried with respect to range of value reported in the aforementioned studies with little modification. Thus, for the processes associated with OM mineralization, our model fitting procedure was constrained to these prior best-fit (Ait Ballagh et al., 2021; Pastor et al., 2011b). Thereafter, the processes affecting the iron and manganese cycle were then parameterized. As these previous modelling studies only capture the anaerobic diagenesis processes by considering a lumped term, ODU (oxygen demand unit), nominal additional parameters pertaining to the coupled iron-sulfur-manganese cycle is derived from other published works (Berg et al., 2003; Dale et al., 2015; Zhao et al., 2020).

However, because the boundary flux for other particulate species besides carbon in the Rhône prodelta sediments is largely unknown, the parameters involving sulfur, iron and manganese interactions were fine-tuned to adapt to the data at hand using both manual and automatic fitting procedures provided by the R package FME (Soetaert and Petzoldt, 2010), while accounting for the constraints present in the study site (e.g low sulfide system (Pastor et al., 2018), high sedimentation rate and carbon flux (Pastor et al., 2011b), low bioturbation (Pruski et al., 2015) and possibly high iron flux (Roussiez et al., 2011).

Table 2: Summary of parameters used in the FESDIA model. (I) independent parameters derived from experiment or field observation external to actual data being simulated (C) constrained parameters obtained from range of literature sources (M) model-derived parameters fitted to the observed data. FDET stands for Fast detritus (labile carbon) and SDET for slow detritus, semi-refractory carbon. Literature sources includes (1) Pastor et al. (2011b), (2) Soetaert et al. (1996), (3) Ait Ballagh et al. (2021), (4) Rassmann et al. (2020), (5) Wang and Van Cappellen (1996) and (6) Wijsman et al. (2002).

Description	Model name	Parameters	Units	Type	Source
total organic C deposition	Cflux	10000	$nmol\ C\ cm^{-2}\ d^{-1}$	I	1
part FDET in carbon flux	pFast	0.5	-	C	1
deposition rate of FeOH3	FeOH3flux	5000	$nmol\ cm^{-2}\ d^{-1}$	M	-
decay rate FDET	rFast	0.05	d^{-1}	C	1
decay rate SDET	rSlow	0.0031	d^{-1}	C	1
NC ratio FDET	NCrFdet	0.14	molN/molC	I	2
NC ratio SDET	NCrSdet	0.1	molN/molC	I	2
upper boundary O2	O2bw	238	$mmol\ m^{-3}$	M	-
upper boundary NO3	NO3bw	0	$mmol\ m^{-3}$	M	-
upper boundary NH3	NH3bw	0	$mmol\ m^{-3}$	M	-
upper boundary CH4	CH4bw	0	$mmol\ m^{-3}$	M	-
upper boundary DIC	DICbw	2360	$mmol\ m^{-3}$	M	-
upper boundary Fe2	Febw	0	$mmol\ m^{-3}$	M	-
upper boundary H2S	H2Sbw	0	$mmol\ m^{-3}$	M	-
upper boundary SO4	SO4bw	30246	$mmol\ m^{-3}$	M	-

Description	Model name	Parameters	Units	Type	Source
upper boundary Manganese	Mnbw	0	$mmol\ m^{-3}$	M	-
advection rate	w	0.027	$cm\ d^{-1}$	M	-
bioturbation coefficient	biot	0.05	$cm^2\ d^{-1}$	C	1
depth of mixed layer	biotdepth	5	cm	I	3
attenuation coeff below biotdepth	biotatt	1	cm	I	3
bio-irrigation rate	irr	0.3	d^{-1}	M	-
depth of irrigated layer	irrdepth	7	cm	I	3
attenuation coeff below irrdepth	irratt	1	cm	I	3
Max nitrification rate step (NH3ox)	rnitri	10	d^{-1}	M	-
temperature	temperature	15.6	dgC	M	-
salinity	salinity	37.8	psu	M	-
refractory Carbon conc	TOC0	1	%	I	5
maximum rate FeS production	rFeS	0.5	$cm^3\ nmol^{-1}\ d^{-1}$	I	4
Max rate anaerobic oxidation Methane	rAOM	30×10^{-6}	$cm^3\ nmol^{-1}\ d^{-1}$	I	1/4
surface porosity	por0	0.83	-	I	1/4
deep porosity	pordeep	0.65	-	M/C	-/5
porosity decay coefficient	porcoeff	2	cm	M/C	-/5
Rate of Sulfide-mediated iron reduction (oxyhydr)oxides	rH2Sfeox	0.00121	$cm^3\ nmol^{-1}\ d^{-1}$	M/C	-/5
Flux of Mn Oxides	MnO2flux	1000	$nmol\ cm^{-2}\ d^{-1}$	M/C	-/5
Rate of Reoxidation of H2S by MnOx	rH2SMnox	0.001728	$cm^3\ nmol^{-1}\ d^{-1}$	C	6
Rate of Reoxidation of Fe with MnOx	rMnFe	6.5×10^{-6}	$cm^3\ nmol^{-1}\ d^{-1}$	C	2

2.4 Characterization of flood dynamics

As introduced in Nmor et al. (2022), the dynamics of the flood deposition events is driven by the characteristics of the sediment delivered (such as the deposit thickness, organic carbon content and reactivity). In that study, the mechanism of flood-induced sediment deposition was modeled as a single massive event against an underlying background variation. However, in this paper, this singular flood prescription is expanded to include multiple events in one simulation run,

thereby allowing a chain of event-driven simulation to be performed with their respective characteristics. As a consequence, the so-called enrichment factor (α) - a scaling parameter linked to the quantity of carbon within the flood layer - becomes a time dependent parameter ($\alpha(t)$) in tandem with the thickness extent of the depositional depth ($Z_{pert}(t)$). This advance in the event-depositional algorithm provides some realism to how natural dynamic sedimentary systems work, albeit with an extra layer of complexity and parameterization constraint to the model.

2.5 Model simulation

2.5.1 Simulation strategies

2.5.1.1 Nominal simulation for flood deposition 2008

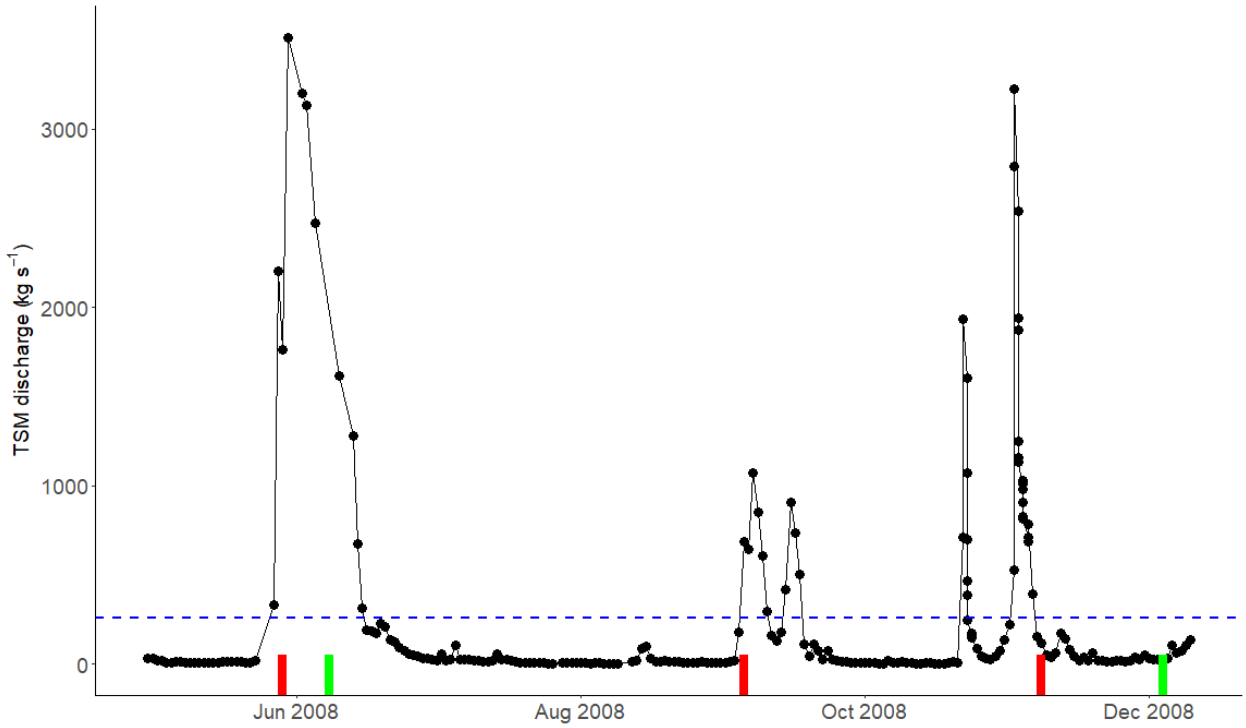

Figure 1: Timeseries of total suspended matter (TSM) river discharge by the Rhône River in year 2008. Red bar denotes the day of deposition used in the model and green bar is the sampling date when measurement was carried out. Blue dashed line is the annual mean of TSM discharge. Data was obtained from the Mediterranean Oceanic Observing System from the Environment (MOOSE database) provided by Mediterranean institute of oceanology.

The numerical procedure for solving the underlying reactive transport equation capturing the processes in Section 2.2 have been previously discussed (Nmor et al., 2022). In summary, the

simulation was carried out in the sediment grid layer of 100 cm thickness with intermittent deposition events treated as an abrupt change to the model dynamics at specified time interval (see Fig. 1).

The model simulation was conducted over two years starting in January 2008 in order to capture the hydrological regime of this particular year. It was started with a steady-state simulation and dynamic spin-up for two years to achieve a dynamic equilibrium. Thereafter, the main simulation was run for two years (January 2008 - December 2009). Because the model can be configured to include multiple events, the decision on when, where, and how many such depositions to implement to adequately describe the observed data was made considering the prevailing hydrodynamical and sedimentological constraints within the sampling time-window (Cathalot et al., 2010; Pastor et al., 2018). We used data from the nearest river monitoring site in Arles (40 km upstream the river mouth) to calculate river discharge and total suspended matter (TSM). Figure 1 depicts the constraints on the timing and magnitude of the deposits. A detailed analysis of the river discharge and the corresponding TSM data suggests a power law relationship (Pont et al., 2002), and examination of the temporal variability in both datasets indicates the occurrence of a minor flood event between the two major deposits (spring and fall deposition) (Fig. 1). Following this analysis, three sequential flood deposition simulations were performed. The first corresponds to a *major* spring flood event with low organic carbon content and a sediment deposition of 30 cm. The second event is associated with a *minor* flood deposits of limited thickness (Cathalot et al., 2010) and organic carbon. The fall flood, which delivered 10 cm of sediment enriched in organic carbon and reactive minerals, was described as the third event (see Cathalot et al. (2010) for sediment deposition in May and November 2008).

Because the intermediate second event was missed by the sampling campaign in 2008, we chose a simple approach by assuming that the event is relatively mild in comparison to the two major floods, as evidenced by discharge and TSM data, as well as down core sediment retrieved in September and October (around the limited deposition event) which show little evidence of deposition (Cathalot et al., 2010). The enrichment factor (α) used in the simulations as well as the thickness of the deposited layer is provided in Table 3. These enrichment factors are basically parameterization of the carbon content in the newly deposited sediment layer relative to the ancient layer and is dependent on the source region of the flood (Nmor et al., 2022).

Table 3: Event specific enrichment factor (α) used in model simulation for spring and fall flood

	C_{org}^{fast}	C_{org}^{slow}	$FeOOH_A$	$FeOOH_B$	MnO_{2A}	MnO_{2B}
Spring	0.5	0.7	0.3	0.3	1	2
Intermediate	0.5	0.7	1.0	1.5	1	2
Fall	20.0	5.0	8.0	2.0	10	5

Furthermore, model analysis performed within this simulation was decomposed into 2 components corresponding to the spring and fall flood event. This calculation was done by integrating any model quantity, variable or metric of interest over a relaxation timescale window. The relaxation interval is defined as the timescale over which a particular variable subject to the perturbation signal caused by flood deposition becomes indistinguishable from background variation (see Nmor et al. (2022) for introduction and Section 2.5.1.2). Thus, the biogeochemical effects of the different flood deposition events can be compared.

2.5.1.2 Relaxation time

The relaxation timescales of the various biogeochemical pathways are calculated in the same way as Nmor et al. (2022). However, a minor change in the methodology is presented using a more analytical rather than numerical approach in order to consider processes or rates which may have a longer timescale of relaxation beyond the interval of two successive deposition. Thus, given that the shape of the so-called "point-by-point" concentration difference between two successive profiles (ϕ) following the perturbation can be approximated as a first order exponential decay:

$$\frac{d\phi}{dt} = -\lambda\phi \qquad (3)$$

a secular rate of decay λ can be estimated from the curve. This is especially true for situations where there is no internal background forcing, such as the configuration investigated in this work. This decay coefficient can be calculated by fitting the distance function $\phi(t)$ to the solution of this exponential decay, such as:

$$\phi = \phi_0 e^{-\lambda t} \qquad (4)$$

where ϕ denotes the point-by-point differences in successive profiles for any given variable/rate for which the relaxation timescale is estimated (see Eq 22 in Nmor et al. (2022)), and ϕ_0 denotes the initial value of the difference between the preflood profile and just after the

deposition. This equation can be used to fit a non-linear regression to determine λ. The distance function's characteristic timescale can then be defined as the timescale over which a fixed percentage of the profile is said to be similar to previous profiles. For example, if the profile has recovered 95% of its pre-flood state, then for all practical purposes, the variable/rate profile in question is more or less indistinguishable from its pre-flood state.

An advantage of this approach is that we can derive an analytical formulation of this relaxation timescale using Eq. 4. For example, a relaxation timescale ($\hat{\tau}_\eta$) for any arbitrary time threshold η can be written as:

$$\hat{\tau}_\eta = \frac{1}{\lambda} ln \frac{100}{100 - \eta} \qquad (5)$$

where τ_η is the relaxation timescale required to restore the system to η % of its preflood state. This analytical derivation allows us to infer the long-term outcomes of these repeated transient responses to constant environmental perturbation. Another advantage of this method is the possibility to investigate the temporal characteristics of the variability of the sediment biogeochemistry if a perturbed system never reaches an ultimate asymptotic state (as in the case of an environment that is sufficiently variable).

2.5.1.3 Memory effect for flood deposition 2008

A natural consequence of the chain of instantaneous flood depositions at various times in the simulation is the possibility of the different biogeochemical processes incorporating a memory effect (i.e. processes at previous time-step might affect processes at future time). Given that relaxation times for some species such as DIC and SO_4^{2-} are up to 5 months (Nmor et al., 2022), they may overlap with other deposition events. The occurrence of these multiple flood deposition events and their interactions could be important drivers of biogeochemical processes in coastal sediment and the resulting fluxes.

We investigate to what extent these sequential flood events might influence the biogeochemical pathways of carbon by conducting another slightly different simulation from the nominal reference simulation detailed above by omitting the first deposition (i.e. spring flood). This provides a way to quantify the changes in the reaction pathways with regard to different situations in a given hydrological year: two successive floods (spring and fall) which relaxation may overlap or one flood only (fall). The comparison of the two situations can provide some suggestion of the possibility of flood-feedback dynamics on the biogeochemistry (Fig. 2).

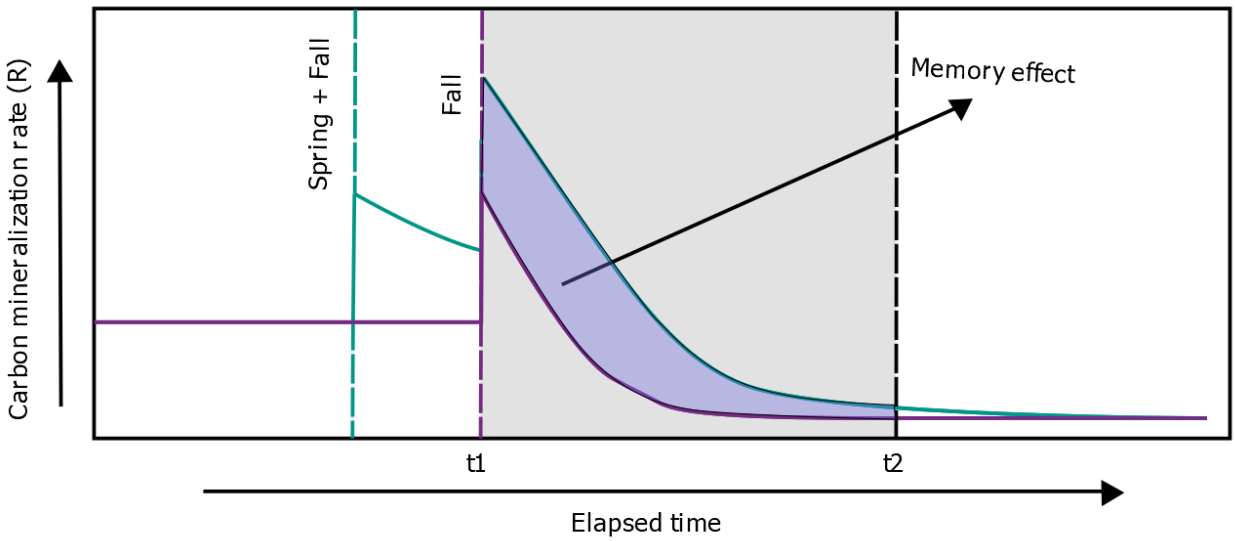

Figure 2: Schematic of the interaction between two floods on biogeochemical process in the sediment. The memory effect of the spring flood on subsequent fall period flood is defined as the time-integrated rate of biogeochemical process between t1 and t2.

Given the occurrence of two characteristic flood events in one hydrological year, we proceeded to diagnose the effect of succession of floods on the biogeochemical rates. To this end, we estimated the memory effect of the flood by simulating two flood events: The first simulation is the same as the simulation performed above where the two depositions occurred within the simulation window, i.e. initialized with spinup profiles and two sequential flood event). The second simulation is performed without the first spring flood (i.e. only second flood effect initialized from the spinup profiles) (Fig. 2). The relative difference in the integrated rates of biogeochemical processes averaged from the start of the fall flood deposition (t1) to the end of the relaxation (t2) in both scenarios indicates the magnitude of the memory effect (ME):

$$ME(\%) = \frac{\int_{t1}^{t2} R^{spring+fall}\, dt - \int_{t1}^{t2} R^{fall}\, dt}{\int_{t1}^{t2} R^{fall}\, dt} \times 100 \qquad (6)$$

where $t1$ and $t2$ is the time interval in which the memory effect of the spring flood on the fall flood is estimated. Each term of the numerator in Eq. 6 is basically the time-integrated difference of any vertical integrated rate biogeochemical process R^i within a time window between $t1$ and $t2$. $t1$ is the fall flood deposition and $t2$ is 6 months later, encompassing the relaxation time of the system. In essence, this numerical experiment implicitly assumed no other intense deposition occurs in between the period when this calculation is performed.

3. Results

3.1 Model-Data evaluation

3.1.1 Global performance of model prediction

The model was validated with the complete data presented in the two flood events in 2008 as described in Pastor et al. (2018) for station A. The skillfulness of the model in describing the observed vertical distributions and their temporal variations was diagnosed using a Taylor diagram (Taylor, 2001), which summarizes the goodness of model fit relative to the data. We considered the depth-dependence variability, model-data bias and model-data correlation as three different measures of the model's performance. The variability is represented by the standard deviation of the observed and modeled values (x and y axis of the graphs) with its magnitude measured as the radial distance from the origin of the plot (dashed line in Fig. 3). A value of 1 indicates a fair representation of vertical variability in the data while value above and below 1 signifies an over or under-estimation of the true variability in the data. The bias measured as the model-data difference (Root Mean Square, RMS) as well as the model standard deviation are normalized by dividing the RMS and standard deviation by the observation's standard deviation (N.sd). The centred root-mean square error (RMSE) is the concentric dashed lines originating from the "observed" point. The further the model is from the observed point, the bigger its bias is. As such, a value close to 0 reflects a good fit of the model to the observation. The "observed" point is plotted on the x-axis at a unit length distance from the origin in this case. As such, we can succinctly visualize, by how much the model fits to the data. This non-dimensional deviation also has the advantage of allowing model-data statistics for different flood types/events to be compared on the same plot. The model-data correlation is captured by the correlation coefficient and is shown on the arc line; with points which lies closest to the x-axis, having the highest correlation.

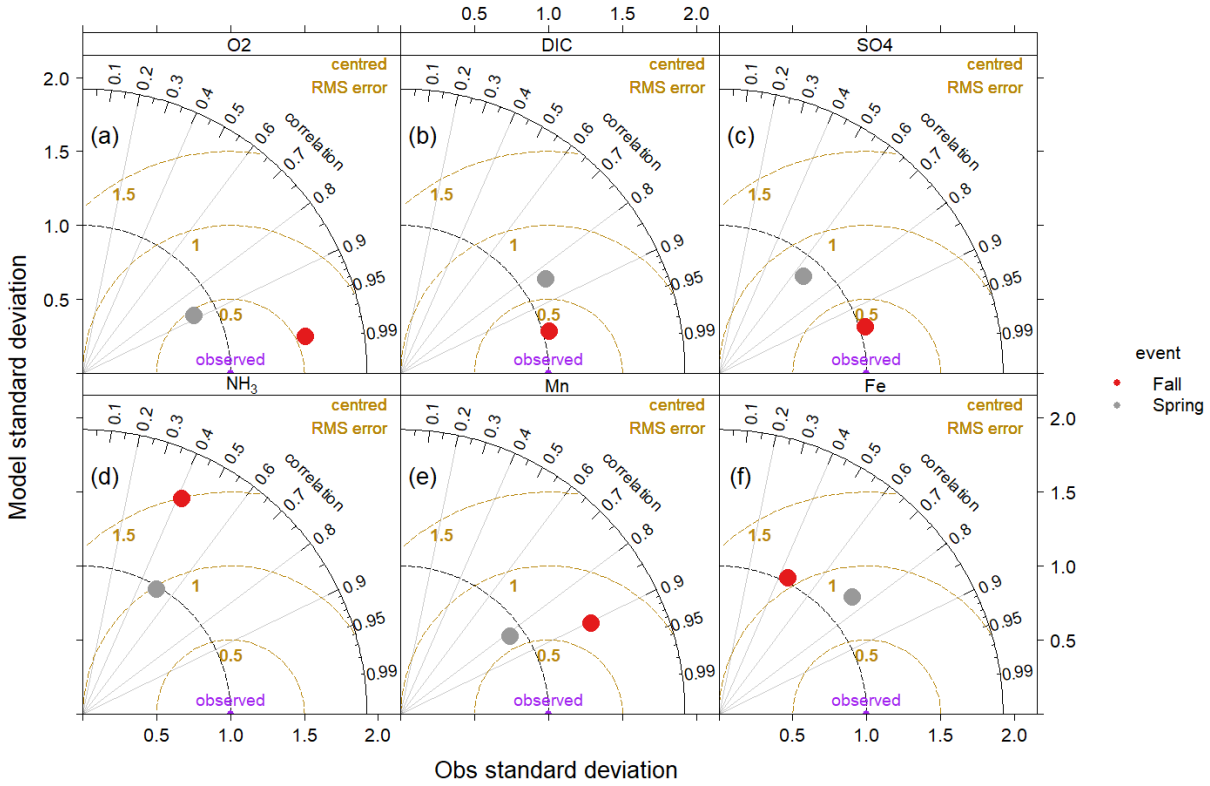

Figure 3: Taylor diagram of Goodness of fit between model simulation and data for (a) Oxygen, O_2 (b) Dissolved inorganic carbon DIC (c) Sulfate SO_4^{2-} (d) Ammonium NH_4^+ (e) Manganese Mn^{2+} and (f) Iron Fe^{2+}. Red and grey dots denote the spring and fall deposition simulation with the normalized observed standard deviation shown in purple. See text for explanation and interpretation.

383 Here, the simulation of oxygen profiles during the spring flood show lesser bias to the oxygen
384 data compared to the fall despite the fact that both events display reasonably high and similar
385 correlations. The model prediction for SO_4^{2-} performed better in both deposition periods with a

correlation of 0.66 and 0.96 for spring and fall flood respectively with a better overall metrics in the fall compared to the spring (Fig. 3). DIC simulated by the model during the fall deposition showed better correspondence with the measured data (high correlation = 0.96) and reasonable representation of the variability in the porewater DIC ($\pm$ 0.5 from true variation i.e half the true variability observed in the data) in comparison to the spring model prediction (Nsd $\pm$ 0.8). Among the reduced metal species, the predicted profile for dissolved Mn was significantly more faithful to the data across both events (with a higher correlation coefficient and lower RMSE) than the predicted profile for dissolved Fe. The vertical variability observed in the fall porewater data is better captured in both cases. Ammonium showed decent model fit with the data in both events with moderate correlation ($r > 0.4$) (Fig. 3).

3.2 Evolution of porewater profiles

3.2.1 Preflood situation

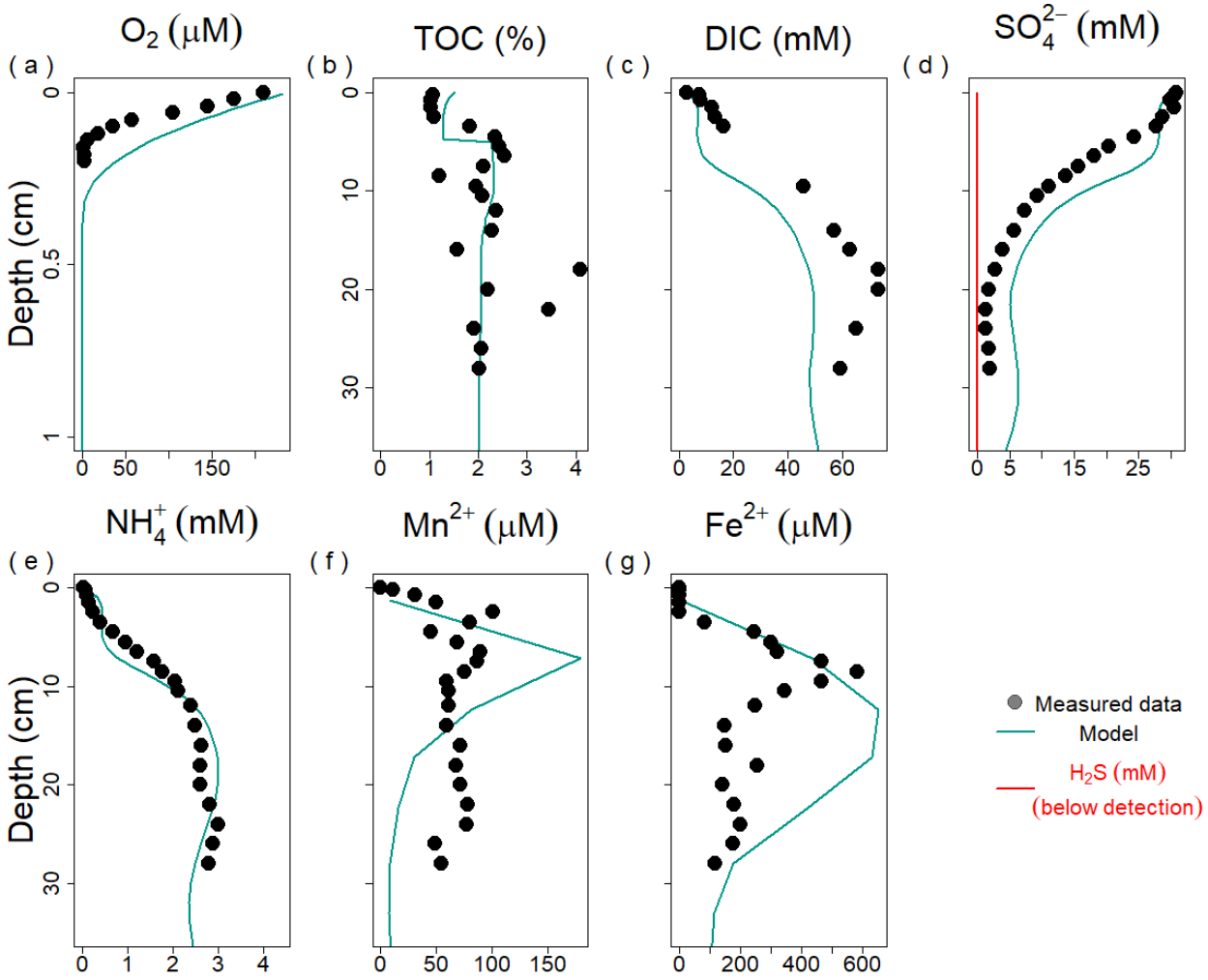

Figure 4: Model data fit against observed data for (a) Oxygen, O_2 (b) Total organic carbon, TOC (c) Dissolved inorganic carbon DIC (d) Sulfate SO_4^{2-} and Hydrogen sulfide H_2S (e) Ammonium NH_4^+ (f) Manganese Mn^{2+} (g) Iron Fe^{2+}. Data collected the 29^{th} of May 2008 at Station A before spring flood (Pastor et al., 2011b).

The porewater profiles prior to the occurrence of the massive flood input in May-June indicated a fairly steady-state condition (Fig. 4). In this preflood situation, the model captured the main biogeochemical features of the prodelta sediment. Simulated TOC profile follows the basic trend in TOC with higher OC content (2%) below 5 cm and high concentration around 20 cm. This variability is typical of sediment accumulation under flood regimes. The deposition of sediment initiated the oxidation of OC which led to a shallow oxygen penetration depth (3.5 mm) before the flood and complete sulfate exhaustion around 20 cm. DIC and NH_4^+ increased with depth to an asymptotic concentration of 60 mM and 3 mM respectively. Furthermore, dissolved Mn was observed with enhanced concentration between 5 and 10 cm with maximum concentration of 100 µM. However, this Mn maximum (179 µM) was overestimated by the model (Fig. 4). The model dissolved Fe profile, on the other hand, demonstrated better agreement with the measured porewater Fe, with a subsurface maximum of 653 µM fed by iron reduction linked to the mineralization of organic carbon-enriched sediment. This peak is however shifted at 20 cm depth in the model versus 10 cm in the data. It is noteworthy that no dissolved sulfide is simulated which reflects the observed absence of sulfide in porewaters.

3.2.2 Generalized flood deposition (Spring 2008)

The delivery of terrestrially-derived sediment particles peaked within ten days after the flood began, with a massive accumulation of sediment as high as 30 cm observed at the study site (Cathalot et al., 2010).

The simulated profiles 10 days after the flood event were able to capture the dominant spatial variation in the porewater species. Given the refractory nature of the deposited sediment, oxygen was present in the surface sediment down to mm (Fig. 5). The model estimate of the oxygen penetration depth is 3.8 mm. Modelled total oxygen flux across the sediment-water interface (SWI) during this period was 13 $mmol\ O_2\ m^{-2}d^{-1}$ while the measured diffusive flux was 9.2 $\pm$ 3.1 $mmol\ O_2\ m^{-2}d^{-1}$. The spatial variation of ammonium was well captured by the model with the low but constant (NH_4^+) at the surface down to the depth of the newly deposited layer (30 cm). However, the model seems to suggest a subsurface peak in NH_4^+ at the former sediment water interface (SWI) which is unobserved in the data.

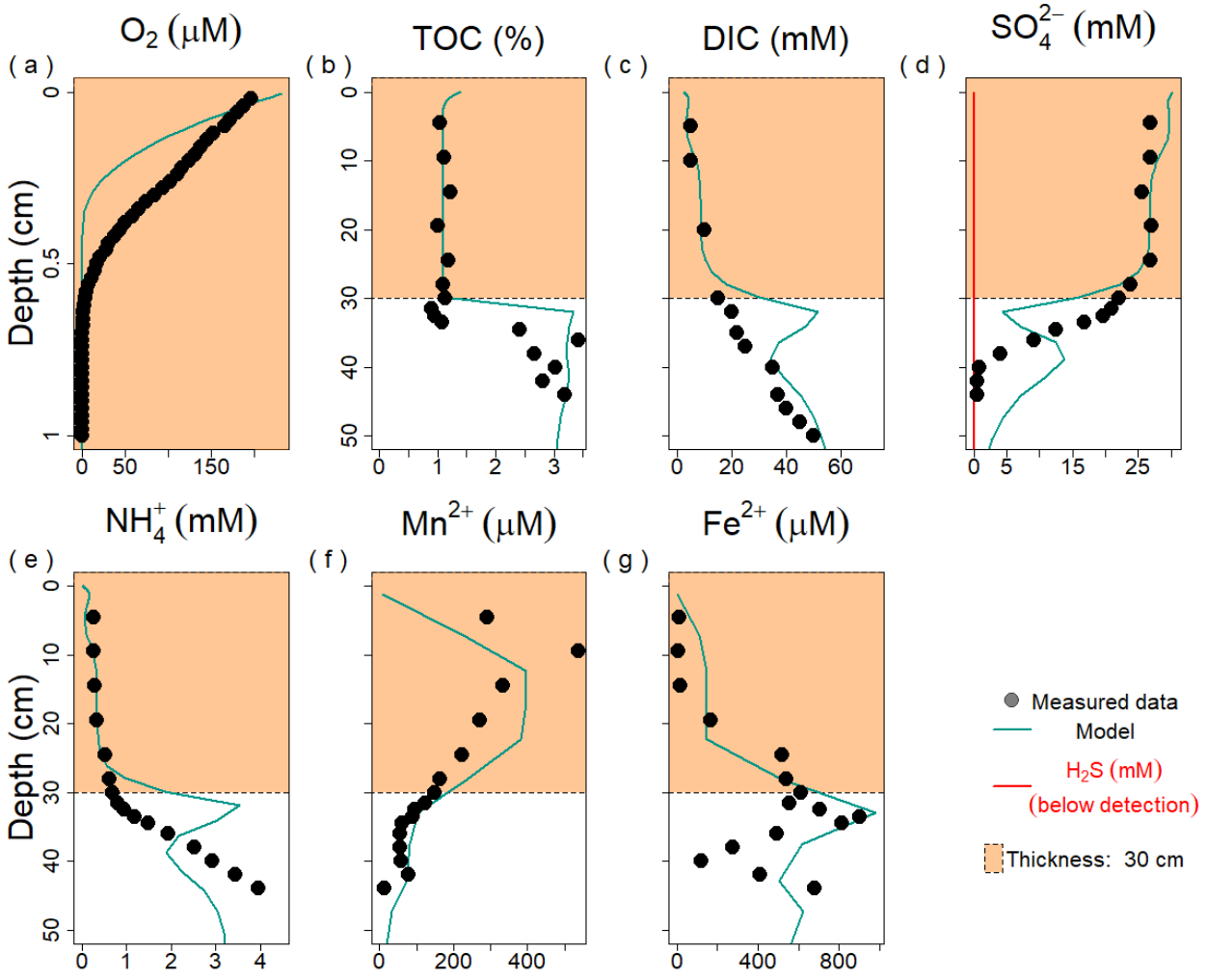

Figure 5: Model data fit against observed data for (a) Oxygen, O_2 (b) Total organic carbon, TOC (c) Dissolved inorganic carbon DIC (d) Sulfate SO_4^{2-} and Hydrogen sulfide H_2S (e) Ammonium NH_4^+ (f) Dissolved manganese Mn^{2+} (g) Dissolved iron Fe^{2+} during the May/June flood. Data were collected the 6^{th} of June 2008 at Station A. The orange section represents the new flood deposit.

Sulfate concentration during this spring event was constant in the upper 30 cm of the sediment, equaling the value of the bottom water concentration trapped in by the flood layer (Fig. 5). Underneath the layer, the sulfate concentration in the model as well as the data decline with depth characterized by strong sulfate reduction (168 $mmol\ C\ m^{-2}d^{-1}$) within this zone. The by-product of this mineralization, dissolved inorganic carbon (DIC) showed a mirrored pattern: with a low but almost constant concentration from the surface down to the depth of 30 cm. Total DIC production beyond this depth was 190 $mmol\ C\ m^{-2}d^{-1}$ and was majorly driven by the relatively

433 rich buried OM below the former interface. As for other compounds, the presence of a
434 subsurface peak in the model is noteworthy. The model-calculated correlation between
435 porewater SO_4^{2-} and DIC indicates that the additional flood deposition induced an enhanced DIC
436 due to the complete exhaustion of SO_4^{2-} and a growing importance of methanogenesis (20
437 $mmol\ m^{-2}d^{-1}$), especially just slightly below the zone of sulfate depletion (45 cm) (Fig. 5).

438 ### 3.2.3 Cenevol flood deposition (fall 2008)

439 The contrasting flood deposition observed in the fall of 2008 and the subsequent evolution of
440 the sediment and porewaters, were well-reproduced by the model. One month after the flood,
441 oxygen penetrated down to a depth of 2.2 mm with stronger oxygen demand due to the labile
442 nature of the deposited OM. The total oxygen uptake rate calculated by the model during this
443 fall flood was higher (21 $mmol\ O_2\ m^{-2}d^{-1}$) in comparison to the spring deposition. DIC
444 increased with depth, with the model matching the spatial variation of the measured porewater
445 DIC. The sulfate concentration decreased from 30 mM at the SWI to about 15 mM at a depth of
446 10 cm (Fig. 6). During this period, sulfate reduction accounted for 94 % with flood-induced
447 mineralization rate of 450 $mmol\ m^{-2}\ d^{-1}$. Below this gradient, SO_4^{2-} was largely constant with
448 porewater concentration of 15 mM (Fig. 6).

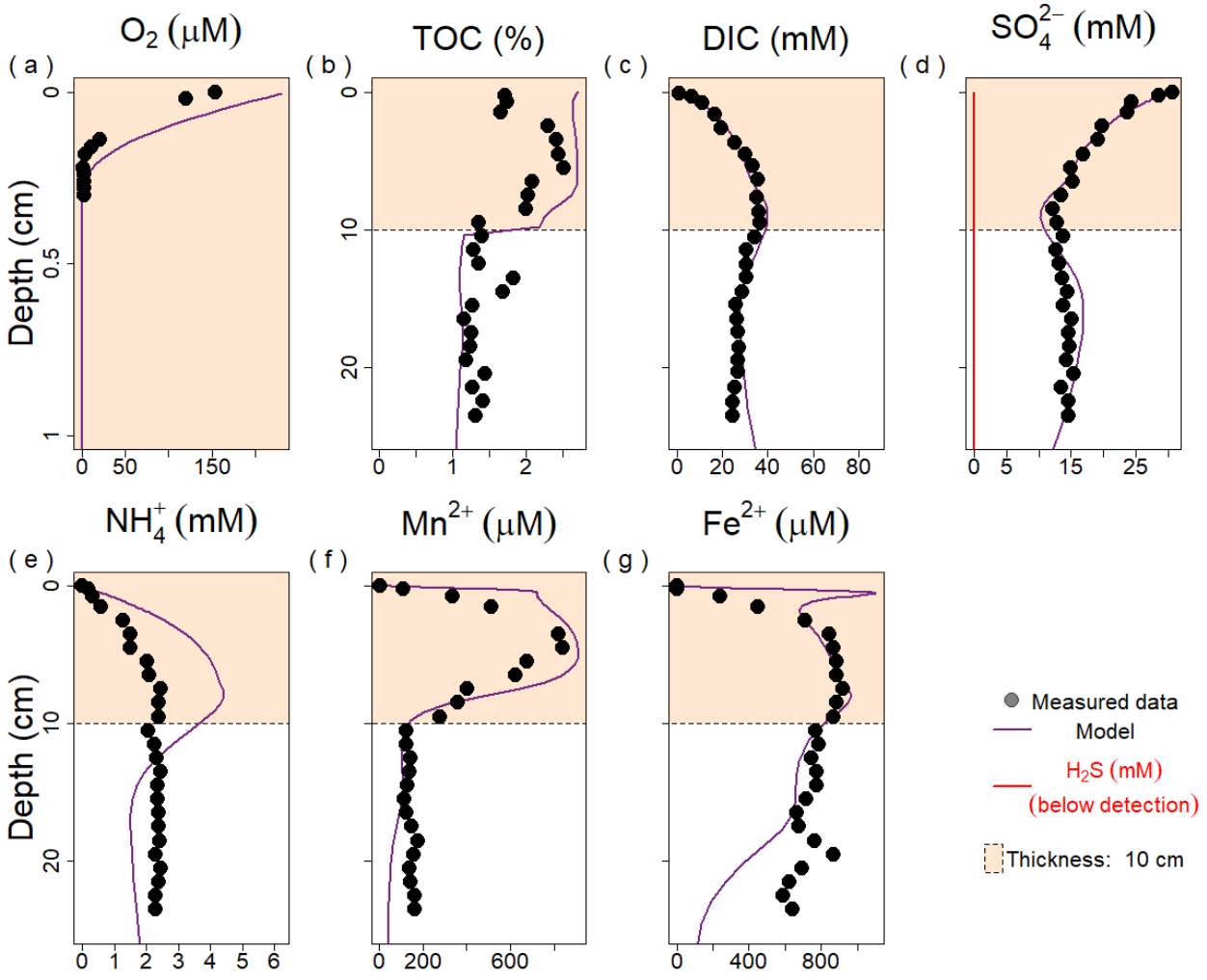

Figure 6: Model data fit against observed data for (a) Oxygen, O_2 (b) Total organic carbon, TOC (c) Dissolved inorganic carbon DIC (d) Sulfate SO_4^{2-} and Hydrogen sulfide H_2S (e) Ammonium NH_4^+ (f) Manganese Mn^{2+} (g) Iron Fe^{2+} during the November flood collected the 8th of December 2008 (26 days after the flood event - 11th of November 2008) at station A.

3.2.4 Fe-Mn cycling under episodic flood event

The difference between the flood deposits of the spring and fall floods can also be revealed in the distribution and concentration of dissolved iron and manganese. A striking feature in the Spring flood is the rapid and large accumulation of Mn in the newly deposited layer (well reproduced by the model) and the depletion of dissolved iron in this same layer, also captured by the model. On the contrary, after the fall flood, the situation, a month after deposition, shows a large accumulation of both dissolved Fe and Mn in the porewaters.

In general, when compared to the measured porewater profiles during the spring flood, the model simulation in the fall event moderately reproduced the vertical structure of the data and suggest a transiently, non-steady state condition of the dissolved Fe and Mn. In order to simulate this different flood deposit, a fixed particulate oxide flux of 50 and 10 $mmol\ m^{-2}\ d^{-1}$ for iron and manganese respectively was imposed in the model upper boundary. The availability of this particulate Fe and Mn as well as organic carbon generates a release of dissolved metals in the porewater. Our model simulation indicates that at the time of sampling in June 2008, the dissolved Mn peak had already migrated from a depth of 30 cm (below the newly deposited layer) and got enriched by a factor of 4 to around 10 cm where the observed Mn maximum was detected (Fig. 5). At this particular depth of 10 cm, the model matches the trend but not exactly the amplitude of the observed variation (data - 537 vs model - 399 µM). Below this reactive front, Mn decrease with depth was observed and simulated. Both the measured data and model prediction suggest a complete reduction of MnO_2 and negligible release of dissolved Mn at depth.

In contrast, dissolved Fe during the spring flood period was comparatively low in the new flood layer in the measured data and increased with depth to a concentration of 980 µM at the former SWI (now buried underneath the deposited layer) (Fig. 5). In this zone, non-steady dynamics was simulated by the model as can be seen in Figure 5, probably driven by a combination of diagenetic processes involving microbial iron oxide reduction, dissolved sulfide reoxidation by Fe oxides and FeS precipitation Eq. 2. This geochemical horizon in the subsurface layer where dissolved Fe is maximum only migrate slowly and persist for a longer period after the spring flood deposition.

In the fall flood, a different vertical profile of the reduced metals emerged. Like the measured data, the model again predicted a large accumulation of dissolved Mn in the flood layer sub-surface Mn peak of 912 µM within the vicinity of 5 cm which shows a good correspondence with the data (840 µM). In contrast to the spring flood where dissolved iron was confined below the new flood layer, Fe^{2+} also accumulated in the fall with a gradual increase from the surface up to 834 µM at 5 cm. This gradient in measured and simulated Fe^{2+} data stabilized to this asymptotic concentration albeit with a tendency of a slight departure from the model (Fig. 6).

Table 4: Depth-Integrated biogeochemical processes associated to Iron and Manganese in spring and fall calculated from time of the event deposition up to a relaxation timescale window of 4 months. Relaxation timescale calculated using Eq. 2.5. Rates are in units of $mmol\ m^{-2}\ d^{-1}$.

Processes	Spring	Fall
Fe		
FeOOH reduction	39.0	44.5
H_2S oxidation via FeOOH	83.0	207.1
Total FeOOH reduction	**122.0**	**251.6**
Fe^{2+} oxidation by O_2	6.1	6.7
FeS production	48.1	94.8
Fe^{2+} oxidation via MnO_2	0.1	0.1
Mn		
MnO_2 reduction	7.2	7.1
H_2S oxidation via MnO_2	19.0	45.0
Total MnO_2 reduction	**26.3**	**52.1**
Mn^{2+} oxidation by O_2	0.3	0.2
$MnCO_3$ precipitation	18.3	27.1

The source of these metals in porewaters is linked to the reduction of iron and manganese oxides which differs from the other oxidants utilized because of the relative importance of microbial-mediated and chemical reduction pathways. Integrating the various biogeochemical processes over a 4 months window linked to the relaxation timescale of iron and manganese shows a sediment that is sufficiently reducing with the dissolved metals accumulating at a faster rate relative to their sink following the event (Table 4). The model calculation suggests that more than two-third of the depth-integrated reduction of $FeOOH$ during the spring deposition is due to the chemical oxidation of H_2S (83 $mmol\ Fe\ m^{-2}d^{-1}$) while it increased to 82 % during the fall flood event (207 $mmol\ Fe\ m^{-2}d^{-1}$) while the depth-integrated rate of microbial iron reduction during the spring flood event (39 $mmol\ Fe\ m^{-2}d^{-1}$) represented a limited amount of FeOOH reduction. The proportion of chemical versus microbial reduction of Mn oxides is similar, showing the importance of sulfide as a reducer for metal oxides in these dynamic conditions.

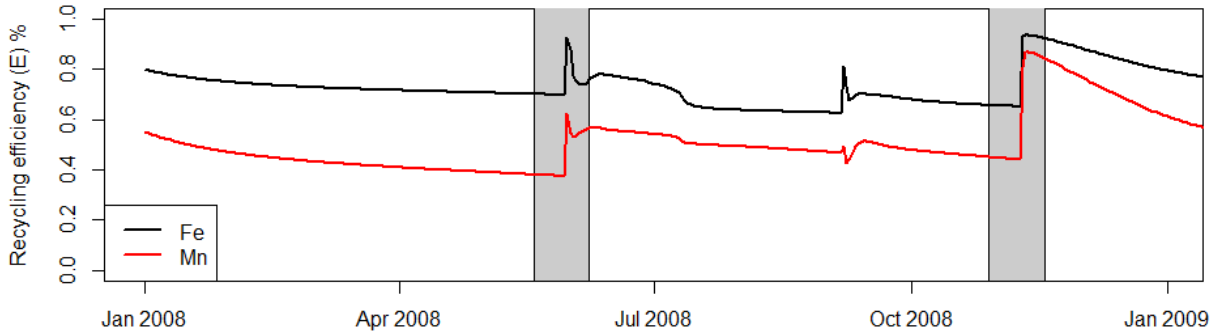

Figure 7: Temporal evolution of recycling efficiency of the metals (iron and manganese) in the sediment. Increasing efficiency numbers imply that the sediment has a high recycling capacity, with a limiting value of 1 indicating that ions cycle only between oxidized and reduced forms inside the sediment without external inputs. The gray bar indicates the time of the flood deposition.

This redox cycling in the sediment can be quantified using the recycling efficiency number, E^i (Eq. 7) (Rabouille and Gaillard, 1991; Wang and Van Cappellen, 1996) adapted for a time dependent model:

$$E^i = \frac{R^i_{red}}{J + R^i_{red}} \qquad (7)$$

where R^i_{red} is the depth integrated rate of Fe or Mn reduction at each time point, i and J is the deposition flux of reactive metal oxides. Values near 1 indicate a very strong internal cycle, whereas values below 0.2 indicate flux dominated metal oxide reduction. Using this calculation, the model suggested that the sediment reactivity is under intense recycling in both flood events (> 0.5) especially after the flood deposition. In this case, the efficiency number jumps from 0.7 to 0.92 for Fe and 0.38 to 0.62 for Mn in the spring. The recycling potential was slightly higher during the fall flood event for both Mn and Fe (0.87 and 0.94 respectively) compared to the Spring flood (Fig. 7).

3.3 Mineralization pathways and biogeochemical fluxes

Following calibration of the model with the data, we extracted timeseries fluxes of dissolved species across the SWI, as well as calculated vertically integrated rates.

3.3.0.1 Exchange across the sediment-water interface

The model indicates that a reduced oxygen consumption follows the introduction of the 30 cm deposit of the spring flood as observed by the oxygen flux across the SWI. Model sediment O_2 flux declined from 18.43 to 8.4 $mmol\ O_2\ m^{-2}d^{-1}$ immediately after the first major deposition; rebounding back within 15 days to its pre-flood level. It is worth noting that this range of O_2 flux encompasses the measured flux snapshot (see: Section 3.2.2 and Fig. 8). The fall perturbation induced a 39 % increase in oxygen flux which relaxes in 40 days. Oxygen consumption was dominated by oxic mineralization accounting for 76 and 71 % of the total oxygen consumption during the spring and fall flood event respectively. Aerobic oxidation of methane doubled between the spring and fall flood accounting for 0.3 and 2 % respectively. This shift in methane reoxidation is caused by the dynamic modification of the sediment, which results in a greater amount of CH_4 produced by different flood types.

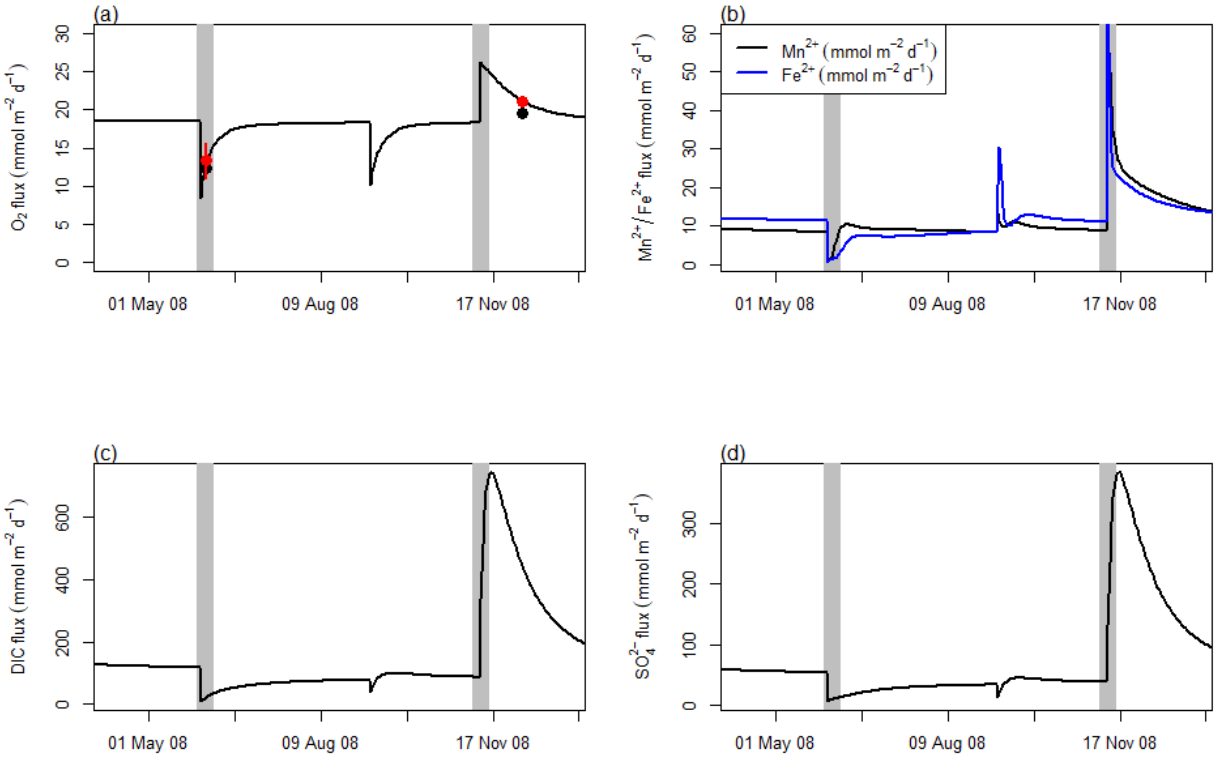

Figure 8: Temporal magnitude of flux (in absolute value) across the sediment-water interface for (a) Oxygen (b) iron and manganese (c) DIC (d) Sulfate. Black dot in O_2 flux signifies measurement made during this sampling point while red dot is the model equivalent as the

measured sampling date. Vertical error bar represents the flux uncertainty in the exact date when this flood occurs. Flux for DIC, Iron and Manganese are directed out of the sediment while Sulfate and Oxygen flux are directed into the sediment. The gray bar indicates the time of the major flood depositions.

Over the same interval, the flux of SO_4^{2-} into the sediment follows the same pattern as above but with a larger increase during the fall flooding where SO_4^{2-} exchange across the SWI first jumped to a very high values (× 7), then decreases, thus temporarily increasing the overall sediment stock of SO_4^{2-} with an increased consumption afterwards. Throughout the simulation period, the sediment was a source of DIC for the bottom water. The DIC exchange showed a strong contrast between the two floods: during the spring depositional event, the DIC flux dropped to a very low value (139 $mmol\ C\ m^{-2}d^{-1}$ to 8 $mmol\ C\ m^{-2}d^{-1}$) whereas it jumped to a much higher efflux estimated after the fall flood (745 $mmol\ C\ m^{-2}d^{-1}$) (Fig. 8).

The magnitude of dissolved Fe and Mn release associated with the spring flood deposit was weakened. In contrast, the sediment acted as a strong source of dissolved Fe and Mn to the bottom water during the fall which can be driven by the reduction of freshly supplied oxides. As this new layer is smaller in thickness in the fall (10 cm), the diagenetic transformations of OM and associated oxides result in an instant enhancement of the sediment inventory of dissolved Fe and Mn (Fig. 8). A burst in Fe and Mn release was simulated immediately after the deposit, which quickly rebounds to its background flux of 11 $mmol\ Mn\ m^{-2}d^{-1}$. For manganese, this stock of reduced metabolites was quickly re-oxidized within the sediment.

544 ***3.3.0.2 Temporal evolution of biogeochemical pathways***

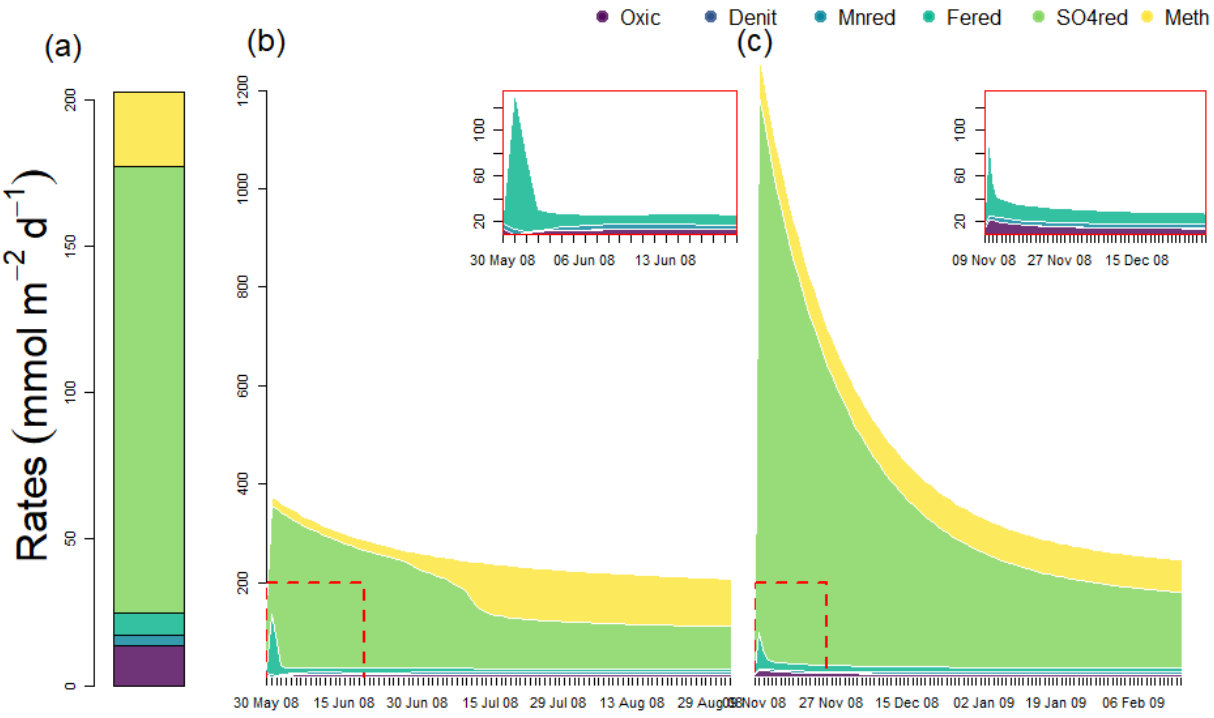

Figure 9: Dynamic evolution of total organic carbon mineralization rate. (a) steady state of total organic carbon mineralization rate and different portion of the mineralization pathways. Oxic = aerobic mineralization, Denit = Denitrification, Mnred = Mn oxides reduction, Fered = Fe oxides reduction, SO4red = Sulfate reduction, Meth = Methanogenesis. (b and c) Dynamic evolution of total organic carbon mineralization rate and relative importance of the carbon biogeochemical pathways following the successive flood in spring (b) and fall (c) period. The beginning date is the day of major flood deposits for each event. The insert zooms in on the pathways with lower carbon mineralization rate.

545 The dynamics of the TOC mineralization and the partitioning in the different biogeochemical
546 pathways are shown in Fig. 9. Before the event, the preflood sulfate reduction (75 %) was the
547 dominant mechanism of carbon oxidation, with minor contribution from aerobic respiration (7 %)
548 and methanogenesis (13 %). The contribution from metal reduction was equally low (3 %).
549 During the first 10 days after the spring flood deposition, oxic mineralization dropped to 5 % with
550 similar marginal change in metal reduction. After this initial drop, aerobic respiration increased
551 up to pre-flood level and stabilized. Similar asymptoticity of reaction rate was observed in metal
552 reduction at short interval after the deposition.

553 The most remarkable change occurring during this flood is observed in the change in anoxic
554 contribution to carbon mineralization rate (sulfate reduction and methanogenesis). The model
555 simulated 50 % increase (227 $mmol\ m^{-2}\ d^{-1}$ versus 151 $mmol\ m^{-2}\ d^{-1}$) in sulfate reduction
556 from its pre-flood rate due to the perturbation while methanogenesis doubled as a result of the
557 deposition (Fig. 9). About 20 days after this spring perturbation, both pathways for total carbon
558 mineralization begins to decline as the signature of the deposition begins to wane. Beyond two
559 months, methanogenesis becomes more prominent equaling the contribution of sulfate
560 reduction.

561 In fall, the large delivery of labile OM produces the greatest change in sulfate reduction
562 (increased from 94 to more than 1000 $mmol\ m^{-2}\ d^{-1}$) and although the rate of methanogenesis
563 almost doubled, the contribution of methanogenesis to total mineralization declined by six-fold
564 from its pre-flood level (Panel b 41 % to 7 % Panel c). During this fall flood, only minor changes
565 in aerobic mineralization as well as metal reduction were simulated except in the very first days.

3.4 Numerical experiment: Memory effect of flood deposition on biogeochemical processes

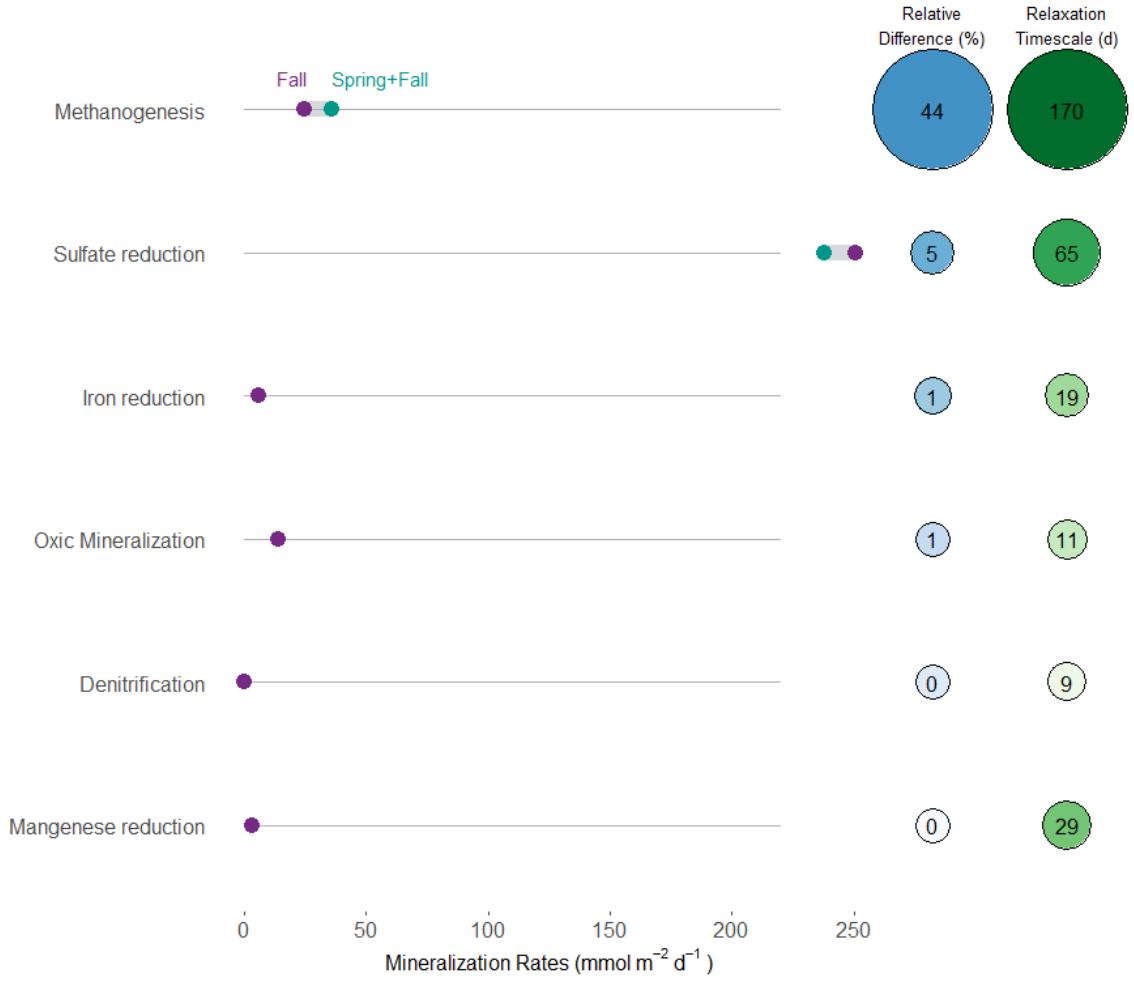

Figure 10: Differential 'memory effect' of flood deposition on biogeochemical pathways of carbon. This is calculated as the relative difference between a reference simulation with both spring and fall flood versus another simulation with only the fall flood (green dots) deposition (purple dots).

We examine the effect of cumulative floods (spring anf fall) compared to a single fall flood. The memory effect is the relative difference of the cumulative fluxes for the two scenarios (see methods). Results from this analysis show that within the time window after the event, the residual effect of the first flood on biogeochemical pathways is large for the anoxic pathways but limited for the other pathways. The succession of two floods lead to limited increase/decrease of mineralization rates for all oxidants between the spring+fall floods scenario compared to second flood (fall event) alone. Our results indicate that methanogenesis has the largest of the residual effect of the flood with memory-induced influence of 44 %. Aerobic mineralization rate shows

little sign of memory effect of the flood deposition (Fig. 10). In similar manner, the relaxation timescale calculated for these processes in the first scenario shows that the recovery period ranges from 6 months for methanogenesis and less than 2 weeks for oxic mineralization.

4. Discussion

In RiOMar systems prodeltas and depocenters are zones of rapid accumulation of sediment along the continent-ocean interface that are typically of terrestrial origin (Blair and Aller, 2012). The quantity and quality of sediment deposited in these depocenters are determined by a variety of parameters, including precipitation pattern in the watershed and river discharge, river network and size, and the sedimentological composition of the watershed from which it originates (Aller, 1980; Chakrapani, 2005). As a result, the materials deposited in the river-ocean margins reflect the source and transit path taken, and so differ in the properties of organic matter supplied in the majority of depocenters (LaRowe et al., 2020).

The amount of organic matter deposited near the river mouth in the Rhône prodelta varies with the flood type. The component of the material deposited in 2008, for example, distinguishes the spring flood from the fall flood (Cathalot et al., 2010). In comparison to the fall flood, which was characterized by labile OM with relatively recent $\Delta^{14}C$ (-90‰ Cathalot et al. (2013)), the spring consists primarily of refractory debris with depleted $\Delta^{14}C$ (-500 ‰), indicating a mix with labile organic matter. These disparities in OM properties can lead to distinct sediment responses, as evidenced by discrepancies in porewater profiles. The difference is reflected in the model by the carbon enrichment factor (α) imposed in both events, with a greater value in the fall compared to the spring (Table 3), indicating that the organic matter delivered during these events can have significantly different features. However, this relationship is not known and certainly complex as other factors like deposit thickness might influence sediment dynamics in response to flood deposition (Nmor et al., 2022). Here we discuss the implication of these flood event deposition and their types on the biogeochemical processes in the sediment.

4.1 Early diagenesis of Rhône prodelta sediments

The Rhône prodelta sediment is a highly dynamic environment driven by episodic flood discharge. This flood-driven phenomenon delivers considerable amounts of sedimentary materials which drives the biogeochemical characteristics of the zone. Integrating observed data with numerical modelling as done here sheds light on the different diagenetic processes that

operate during periods of flood-induced organic matter input. However, this data-driven modelling approach can only be validated by the fidelity of the model in capturing the observed trend and variability present in the data. In this study, we provide some objective metrics to assess the skillfulness of the numerical model in reproducing the spatio-temporal pattern of the dataset (Fig. 3). Our findings demonstrate that the model porewater profile for sulfate, DIC and manganese were well represented in both flood events in term of their adjustments to the data as well as the variability with depth.

In contrast, despite their correlation with the data, the overall model skillfulness of the simulated results for ammonium and iron during spring deposition is less impressive. This is especially true for iron, where the vertical variability of the porewater profile suggests a system still in the process of slow evolution that is tightly coupled to other cycles (Fig. 5). With more data constraints for such evaluation (i.e. FeOx and MnOx deposition flux and reactivity), the model's performance could be improved through better characterization of the Fe dynamics during this time period. The lesser known dynamics and forcings (transient phases, OM lability) at the start of the perturbation, as well as the uncertainty about when this specific event occurred, may also be responsible for the bias in the May-June flood. Furthermore, our preliminary test carried with and without the inclusion of an intermediate flood deposition (around September) between the two events highlights the important of data coverage and timescale of investigation for capturing the key features of the interstitial porewater signature arising from this type of event (Romans et al., 2016).

Moreover, the model-data assessment showed much better fit in the fall flood suggesting that the model is not far off from describing the general pattern in sediment dynamics during this flood year. Furthermore, the O_2 flux temporal patterns have been well-studied in this region in 2008 and shows temporal variability linked to extreme events (Cathalot et al., 2010). Our model O_2 flux (accounting for both diffusive and irrigative flux) in both flood event slightly overestimate the observed diffusive oxygen uptake (DOU) flux reported in Cathalot et al. (2010) and Pastor et al. (2018) for this particular prodelta site but much closer to the average TOU observed in this site (about 24 $mmol\ C\ m^{-2}d^{-1}$) (Lansard et al., 2008, 2009; Pastor et al., 2011a). This range of oxygen flux compared favorably to other RiOMar systems characterized by high sedimentation rate and particulate carbon flux: Amazon delta (6 - 25 $mmol\ C\ m^{-2}d^{-1}$ Aller et al. (1996)), Mississippi delta (2 - 56 $mmol\ C\ m^{-2}d^{-1}$ Morse and Rowe (1999)) and other coastal areas with pulse cycle of resuspension and deposition such as in Göteborg harbour, Sweden (8 - 23

639 $mmol\ C\ m^{-2}d^{-1}$ Tengberg et al. (2003)), Gulf of Finland, Baltic sea (5 - 20 $mmol\ C\ m^{-2}d^{-1}$
640 Almroth et al. (2009)), Gulf of Mexico (7 - 50 $mmol\ C\ m^{-2}d^{-1}$ Moriarty et al. (2018)).

641 Within the Rhône prodelta, the sediment biogeochemical dynamics is closely coupled to the
642 underlying transport and biogeochemical changes linked to massive depositional event. As in
643 the case described in the fall flood, a strong oxygen consumption ensued in the first few days
644 after the events via immediate degradation of organic carbon driven by oxic mineralization. Our
645 model in agreement with the data showed substantial temporal variability in the O_2 flux driven by
646 the variability in organic carbon input associated with the flood event. Especially, the lowering of
647 O_2 fluxes observed after the spring flood is well represented by the model. Organic carbon
648 mineralization in general was dominated by sulfate reduction in both spring and fall events. In
649 both cases, the total mineralization increased by a factor of 2 in spring and 7 in winter reflecting
650 the amount and lability of the OM deposited with a much larger increase of the total carbon
651 mineralization during the fall depositional event compared to the spring one. During the spring
652 event, a significant portion of the total mineralization was induced at the old sediment-water
653 interface where a layer of degradable organic matter was buried by the flood deposit. This layer
654 is located at 30 cm depth after the flood, therefore lowering the transfers at the present
655 sediment-water interface. This organic-rich material fuels the intense subsurface sulfate
656 reduction. Similar trapping and enhanced biogeochemical activities have also been reported in
657 flooded organic rich sediment in the Saguenay fjord (Deflandre et al., 2002; Mucci et al., 2003).

658 This trend, however, was in contrast with the fall flood where the majority of the mineralization
659 took place in the first 10 cm of the sediment. This is the result of the deposition of organic-rich
660 material during this fall flood. As a result of this dissimilar pattern, DIC production revealed that
661 with organic-rich sediment deposition, particularly during the fall period, a strong DIC efflux
662 across the sediment-water interface (445 $mmol\ DIC\ m^{-2}d^{-1}$) can be expected. On the contrary
663 in spring, recycling is internal (below the 30 cm flood layer) and leads to reduced exchange with
664 the water column. While benthic release of DIC in this proximal zone of the Rhône delta is not
665 as frequently measured as oxygen flux (and especially in the flood period), reported
666 measurement estimate that DIC flux ranges between 18 and 78 $mmol\ DIC\ m^{-2}d^{-1}$ before the
667 usual flood season of late summer (Rassmann et al., 2020). As the model is dynamic in time
668 and linked by successive episodic flood event, an hindcast of DIC flux before this flood season
669 showed better correspondence (55 $mmol\ DIC\ m^{-2}d^{-1}$) with reported values for this site.

670 Short term dynamics in manganese and iron redox cycling was assessed with the model
671 constrained by the available data and empirical observations at this proximal site. The

672 porewater chemistry in the prodelta was altered by the spring (generalized) and fall (cevenol)
673 floods, with differing responses for Mn and Fe. Model Mn oxides reduction rate was estimated
674 around 26 $mmol\ Mn\ m^{-2}d^{-1}$ in the spring compared to 52 in the fall. Chemical reduction via
675 oxidation of sulfide accounted for about 72% while microbially mediated reduction of organic
676 carbon accounted for 28% during the spring deposition. The latter had a much lower
677 contribution in fall (14%) compared to the spring event with a stronger contribution by H_2S
678 oxidation via Mn oxides. This fall enrichment of dissolved Mn in the upper sediment layer (up to
679 800 µM Fig. 6) also seen in the Saguenay fjord after a large depositional event (Deflandre et al.,
680 2002) is driven by the strong imbalance between the sources and sinks (Table 4) resulting in its
681 unique shape with the contribution from the reoxidation of dissolved Fe^{2+} by MnO_2 as the major
682 driver. In contrast, dissolved iron porewater profile is primarily controlled by the reoxidation of
683 sulfides (68 %). However, in the fall event, this large iron release is balanced in deeper layers
684 by precipitation to a stable form of FeS and lost by burial to deeper layers. This dynamic
685 diagenetic balance could be responsible for the peculiarity of the observed pattern of the
686 dissolved iron profile (Fig. 5). Indeed, other previous studies in the Rhône prodelta have alluded
687 to this routing of iron-sulfide precipitation as a possible mechanism for the maintenance of the
688 observed ferruginous condition and the alkalinity fluxes (Pastor et al., 2018; Rassmann et al.,
689 2020).

690 Furthermore, recent research by Van de Velde et al. (2020) has demonstrated that oscillating
691 redox circumstances can affect remineralization processes where a dominating Fe state with
692 regard to sulfide can occur due to the sediment's inherent bistability. This bistability condition is
693 determined by the particulate carbon to iron input ratio. In our example, with significant carbon
694 (Ait Ballagh et al., 2021; Pastor et al., 2011b) and iron flux (Marin and Giresse, 2001;
695 Radakovitch et al., 2008; Roussiez et al., 2011), this ratio is 5, and such Fe-rich and sulfide-free
696 condition is observed, as theoretically predicted by Van de Velde et al. (2020) when combined
697 with kinetically fast FeS formation as in the natural environment. Thus, our results highlight the
698 suggested possibility of chemical reduction of the metal oxides as well as precipitation of FeS
699 (and subsequent pyrite formation) (Pastor et al., 2011b; Rassmann et al., 2020). These
700 secondary reactions (especially chemical reduction of manganese oxide by reduced iron) may
701 help explain the elevated Mn^{2+} concentration in the sediment after both floods with higher
702 values in the fall (Pastor et al., 2018).

703 In general, the high metal reduction is a consequence of two factors: Firstly, the large deposition
704 of terrigenous materials linked to high sedimentation rate and possibly large concentrations of

reducible iron terrestrially transferred to this depocenter (Pastor et al., 2018; Roussiez et al., 2011) as implied by the relatively higher α value imposed in November deposit in order to simulate such observed trend. Secondly, the importance of secondary reactions involving cycle of Fe and Mn as an efficient metal cycling in the area (Fig. 7). This view of metal cycling has also been previously suggested to be responsible for the rapid recycling of manganese and iron in the seafloor (Rabouille and Gaillard, 1991; Van Cappellen and Wang, 1996; Wang and Van Cappellen, 1996). The second factor could be critical after flood deposition during the most dynamic part of the transient state in maintaining the dominance of dissolved reduced metals in porewaters as observed in Figure 5 and Figure 6 and the absence of $\sum H_2S$ in the porewater (Pastor et al., 2011b). This modelling insight on the role of combined factor in redox cycle of metals is also supported by observation in other dynamic sedimentary systems subject to episodic flood events (Blair and Aller, 2012).

4.2 Implication of intense flood deposition in biogeochemical cycle

As discussed previously, river dominated margins serve as retention zones for riverine borne particulate matter and are subject to both anthropogenic and natural perturbation (Dai et al., 2022). These extreme events bring large quantities of sediment within a short timeframe which has the possibility to induce changes in the biogeochemical properties of the sediment. In the Rhône River prodelta, the annual flood can deliver up to 5.4×10^6 tons of sediment in 10 days period (Antonelli et al., 2008). This large volume of sediment delivered is also seen in similar river systems with rapid sedimentation of riverine materials: Pô river flood in 2007 (Miserocchi et al., 2007), Saguenay Fjord, Canada (landslide - Deflandre et al., 2002; Mucci and Edenborn, 1992). Thus, the introduction of these new materials can affect not only the carbon cycle but also the other elemental cycles such as iron and manganese as demonstrated in this paper.

Under this flood regime, biogeochemical processes undergo sudden change linked to biogeochemical conditions in the sediment. For example, the oxygen flux decreases by 55 % during the spring flood event and depending on the prevailing characteristics of the particulate input, strongly anoxic condition with greater propensity for methanogenesis can be induced. Our result shows that this is the case for pathways affecting the carbon cycle where sulfate reduction and methane production can double or even quadruple at short time interval following these massive sediment depositions. The substantial changes in carbon mineralization results to enhanced DIC production and can have a considerable effect on DIC flux across the sediment-water interface. Our findings reveal that the intensity of DIC exchange varies with the flood type, with a much higher flux of DIC in the fall compared to the spring, reflecting the

738 contrast in the nature of materials deposited. Such abrupt changes in the recycling of carbon in
739 the sediments has been observed in other region where the seafloor is disturbed by
740 anthropogenic forcing such as disposal activities and dredging where average OC
741 mineralization rate can be enhanced by a factor 2.5 (Van de Velde et al. (2018)).

742 Furthermore, the difference in DIC flux simulated by these floods indicates that different carbon
743 cycling mechanisms are at work in the deposited materials. According to the model, the spring
744 deposition resulted in an internal production and porewater storage of the DIC, possibly due to
745 the mineralization of trapped reactive materials buried beneath the newly deposited refractory
746 layers. This resulted in a decrease in exchange across the SWI. Mineralization of carbon-rich
747 OM in the fall resulted in a significant and rapid increase in DIC release in the flood layer and an
748 increased exchange with the bottom water. These two dissimilar responses demonstrate that
749 these floods might have a diverse impact on material exchange with the water column, which
750 has a considerable impact on coastal carbon dynamics (Bauer et al., 2013; Cai, 2011).

751 We can appreciate this differential response of the coastal sediment to episodic carbon input by
752 means of an integrated view of DIC in terms of the ratio of efflux (Fig. 8) out of the sediment and
753 accumulation (Fig. 5 and Fig. 6) in the porewater. Assuming that the DIC flux trended toward a
754 value before the flood with a timespan associated with the relaxation timescale for DIC (~ 4
755 months Nmor et al. (2022)) and accumulation of porewater DIC within the new flood layer
756 represents a significant share of DIC produced during the OC mineralization, we can provide a
757 synthesis of how these flood events affect the short term dynamics of DIC. This is shown in
758 Figure 11. We observed that during the spring flood, DIC flux out of the sediment integrated and
759 averaged over 4 months was 68 $mmol\ m^{-2}\ d^{-1}$ whereas in that same timeframe, about 30
760 $mmol\ m^{-2}\ d^{-1}$ of DIC accumulate in the sediment interior. This amount to a flux/accumulation
761 ratio of 2 in the spring. In contrast, the fall deposition presented a different picture with a higher
762 efflux to accumulation ratio of about 100 (285/3). This burst of DIC out of the sediment column
763 in response to the intense recycling of carbon in organic-rich sediments deposited with the flood
764 led to little accumulation in the sediment. The conclusion we can draw from here is that these
765 different type of flood events could instantiate two modes of carbon cycling in sediment: an
766 internal cycling driven by large accumulation of DIC in the sediment interior versus an interface
767 cycling characterized by strong flux out of the sediment (Rabouille et al., 2021).

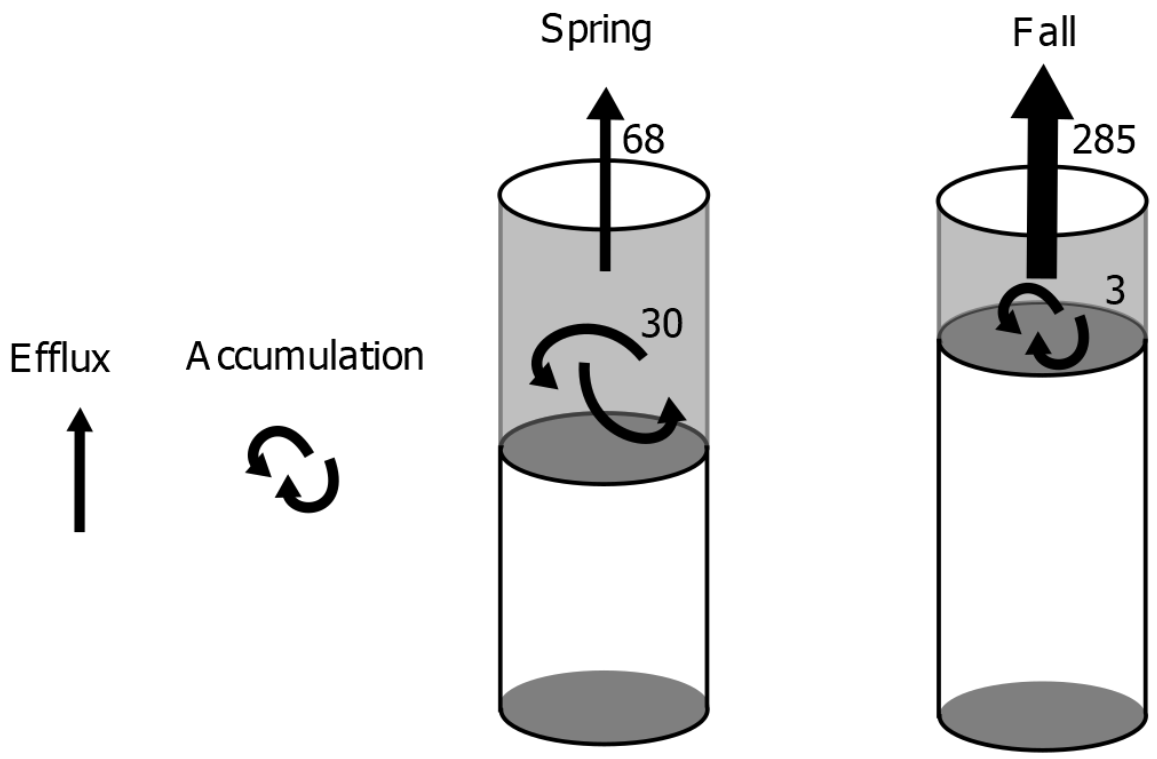

Figure 11: Synthesis of DIC dynamics for the Spring (left) and Fall (right) depositional events. The calculation is made over the relaxation timescale (rts) of 4 months. The accumulation of DIC in the porewater was estimated by the change in inventory of DIC over the depth of the new deposit between the preflood time vs postflood time and divided by the relaxation time (Δt_{rts} = 4 months) i.e. $\frac{1}{\Delta t_{rts}}\left(\int_0^{zpert} C\,(t_{event+rts})dx - \int_0^{zpert} C\,(t_{event})dx\right)$*. The DIC flux out of the sediment was calculated using modelled result in Section 3.3.0.1 integrated and averaged over the relaxation timescale i.e.* $\frac{1}{\Delta_{rts}}\int_{t_{event}}^{t_{event+rst}} D\,IC_{flux}dt$*. All units are in* $mmol\ m^{-2}\ d^{-1}$*.*

In addition, the sediment acting as a bioreactor for exchange of flux of dissolved metals can change depending on the characteristics of the flood type: serving as a large source of iron and manganese during the organic-rich fall flood event and a reduced to insignificant source during the spring flood that is characterized mostly of refractory material. This exchange of flux when coupled to other elemental pathways, such as phosphate can play a role in the retention and mobilization of phosphorus in marine sediment (Reed et al., 2011; Slomp et al., 2013). Massive sediment deposition can also trigger changes in metal recycling efficiency of the sediment. This can result in a diagenetic response of iron and manganese which has consequences on the

776 long-term fate of their respective cycle. For example, metal reduction during non-steady state
777 condition have been shown to be a source of dissolved organic carbon (Deflandre et al., 2002).
778 Furthermore, some of the reduced Fe within the sediment column is sequestered with sulfides
779 which can be critical for the perennial burial of sulfur in the sediment (Jørgensen et al., 2019).
780 This might be the case in deltaic systems connected to river mouths which are dominated by
781 anoxic diagenesis, with intense sulfate reduction and iron oxide reduction which generates an
782 efficient precipitation and burial of FeS/FeS_2. This is actually the scenario for the Rhône prodelta
783 sediment. This precipitation of particulate FeS (FeS_p) have also been detected in the proximal
784 and prodelta stations which indicates that the immobilization of iron bound sulfide could well be
785 active in this sediment and be related to a large alkalinity release (Rassmann et al., 2020).
786 Flood inputs can deeply modify the internal Fe/S cycling, favor FeS production and contribute to
787 reduced species burial, thus controlling alkalinity fluxes to the water column (Rassmann et al.,
788 2020).

789 ### 4.3 Interaction between successive floods

790 As our understanding of rapidly accumulating sedimentary system continues to improve as a
791 result of better observing systems (Maillet et al., 2006; Toussaint et al., 2014; Viollier et al.,
792 2003; Zebracki et al., 2015) and greater appreciation for the non-stationarity in benthic
793 biogeochemical processes (Mucci et al., 2003; Nmor et al., 2022; Pastor et al., 2018; Tesi et al.,
794 2012), the influence of successive depositions of OM materials via these extreme flood events
795 needs to be investigated. One widely recognized consequence of this phenomenon is the
796 decoupling of oxygen consumption from carbon mineralization during transient flood condition
797 (Aller, 1998). Another ramification of this back-to-back occurrence of flood deposition is the
798 cumulative impact induced on the biogeochemical processes. This is demonstrated in our
799 experimental simulation (Fig. 10) where the co-occurrence of sequential flood deposition
800 initiates a temporal lag in the carbon mineralization pathway. Interestingly, the memory effect is
801 visible only for the slow relaxing species (methane). For sulfate, the memory effect is limited
802 because its relaxation time nears 5 month which is the interval between the two floods in 2008.

803 The successive use of terminal electron acceptors for the breakdown of organic matter in the
804 sediment appears to have an intriguing side effect related to these series of flood and follows in
805 the opposite direction of their energy yield (Froelich, 1988). As such, anaerobic processes
806 (methanogenesis and sulfate reduction) have a longer memory lag brought forth by the
807 sediment deposition. This might be the case because the activities involving this pathway take
808 place significantly deeper in the sediment generating a longer relaxation time dictated by their

longer diffusive time (Nmor et al., 2022). Such timescale-dependent recovery of the mineralization pathways has also been attributed to either the depletion of electron acceptors or colonization due to microbial community (Van Velde et al. (2018)). In general, our results show that episodic events such as those observed in the Rhône prodelta and other similar regions can lead to transient states within a perturbation window (Velde et al., 2018). Although in the scenario explored here, the interval between the flood input are far apart for the effect to be consequential and thus the system might have been reset (Fig. 10). The possibility of this "memory effect" on the carbon mineralization pathways and even in other cycles will therefore raise a pertinent question: To what extent does increasing frequency and magnitude of the flood deposition influence the biogeochemical functioning of the coastal sediment especially in the context of changing environmental forcings? Further investigation on the role of this flood-modulated interaction should be conducted to ascertain the biogeochemical implication of this phenomenon.

5. Conclusion

Floods in the river-ocean continuum can deposit sediment materials of several tens of centimeters in a short period of time. As particulate OM is tightly coupled to carbon mineralization in the Rhône River prodelta sediment, this study focuses on two unique flood depositions with variable sediment characteristics (thick organic-poor in spring and thin organic-rich in fall), resulting in distinct biogeochemical responses. The labile nature of the OM provided during the 2008 fall season leads to a much higher increase in organic carbon mineralization when compared to the spring flood. The diagenetic pathway supporting this OC mineralization increase was mostly sulfate reduction as indicated by changes in porewater profiles of sulfate and DIC between the two flood. The different nature of the two floods induced opposite effects on DIC release from sediments with burst of DIC release in the fall versus a decrease of DIC efflux in spring. This highlights the importance of internal vs near surface recycling of carbon in controlling the solute exchange across the SWI. Despite substantial sulfate reduction, no dissolved sulfide was detected in the porewater, indicating strong precipitation with Fe and, eventually, reoxidation with manganese/iron oxides. The model supporting this paradigm emphasizes the involvement of secondary redox mechanisms during non steady-state (representing > 75% of metal reduction) in sustaining the observed profiles in both flood situations. In addition, the sequential accumulation of sediment can also trigger an interaction between two independent flood deposition if the frequency of their occurrence is high enough to

cause an overlap between them. In this case, we demonstrated that anoxic mineralization processes such as sulfate reduction and, in particular, methanogenesis can be influenced by this consecutive flood if it occurs more frequently in the future.

Acknowledgments

This research has been supported by a grant from INSU EC2C0 DELTARhône, by the PPR-RiOMAr project, a French government grant managed by the Agence Nationale de la Recherche under the France 2030 program, reference ANR 22 POCE 0006 and a PhD grant from Ecole doctorale des Sciences de l'Environment, Ile de France (SEIF) N° 129.

Data Availability statement

All simulations is carried out with an early diagenesis model including Iron, sulfur and methane dynamics (FESDIA). The source code for the application used in this publication and the setup configuration can be obtained via github (stanleesocca/GMD-FESDIA (github.com)).

Reference

Ait Ballagh, F. E., C. Rabouille, F. Andrieux-Loyer, K. Soetaert, B. Lansard, B. Bombled, G. Monvoisin, K. Elkalay, and K. Khalil (2021), Spatial variability of organic matter and phosphorus cycling in rhône river prodelta sediments (NW mediterranean sea, france): A model-data approach, *Estuaries and Coasts*, *44*(7), 1765–1789.

Aller, R., N. Blair, Q. Xia, and P. Rude (1996), Remineralization rates, recycling, and storage of carbon in amazon shelf sediments, *Continental Shelf Research*, *16*(5-6), 753–786.

Aller, R. C. (1980), Diagenetic processes near the sediment-water interface of long island sound. I.: Decomposition and nutrient element geochemistry (s, n, p), in *Advances in geophysics*, vol. 22, pp. 237–350, Elsevier.

Aller, R. C. (1998), Mobile deltaic and continental shelf muds as suboxic, fluidized bed reactors, *Marine Chemistry*, *61*(3-4), 143–155.

Allison, M. A., M. T. Lee, A. S. Ogston, and R. C. Aller (2000), Origin of amazon mudbanks along the northeastern coast of south america, *Marine Geology*, *163*(1-4), 241–256.

Almroth, E., A. Tengberg, J. H. Andersson, S. Pakhomova, and P. O. Hall (2009), Effects of resuspension on benthic fluxes of oxygen, nutrients, dissolved inorganic carbon, iron and manganese in the gulf of finland, baltic sea, *Continental Shelf Research*, *29*(5-6), 807–818.

Antonelli, C., F. Eyrolle, B. Rolland, M. Provansal, and F. Sabatier (2008), Suspended sediment and 137Cs fluxes during the exceptional december 2003 flood in the rhone river, southeast france, *Geomorphology*, *95*(3-4), 350–360.

Bauer, J. E., W.-J. Cai, P. A. Raymond, T. S. Bianchi, C. S. Hopkinson, and P. A. Regnier (2013), The changing carbon cycle of the coastal ocean, *Nature*, *504*(7478), 61–70.

Bentley, S. J., and C. A. Nittrouer (2003), Emplacement, modification, and preservation of event strata on a flood-dominated continental shelf: Eel shelf, northern california, *Continental Shelf Research*, *23*(16), 1465–1493.

Berg, P., S. Rysgaard, and B. Thamdrup (2003), Dynamic modeling of early diagenesis and nutrient cycling. A case study in an artic marine sediment, *American journal of science*, *303*(10), 905–955.

876 Bianucci, L., K. Balaguru, R. W. Smith, L. R. Leung, and J. M. Moriarty (2018), Contribution of hurricane-induced
877 sediment resuspension to coastal oxygen dynamics, *Scientific reports*, *8*(1), 1–10.

878 Blair, N. E., and R. C. Aller (2012), The fate of terrestrial organic carbon in the marine environment, *Annual review of*
879 *marine science*, *4*, 401–423.

880 Bonifácio, P. et al. (2014), Spatiotemporal changes in surface sediment characteristics and benthic macrofauna
881 composition off the rhône river in relation to its hydrological regime, *Estuarine, Coastal and Shelf Science*, *151*, 196–
882 209.

883 Bourgeois, S., A. Pruski, M.-Y. Sun, R. Buscail, F. Lantoine, P. Kerhervé, G. Vétion, B. Rivière, and F. Charles
884 (2011), Distribution and lability of land-derived organic matter in the surface sediments of the rhône prodelta and the
885 adjacent shelf (mediterranean sea, france): A multi proxy study, *Biogeosciences*, *8*(11), 3107–3125.

886 Bourrin, F., P. L. Friend, C. L. Amos, E. Manca, C. Ulses, A. Palanques, X. D. De Madron, and C. E. Thompson
887 (2008), Sediment dispersal from a typical mediterranean flood: The têt river, gulf of lions, *Continental Shelf Research*,
888 *28*(15), 1895–1910.

889 Burdige, D. J. (1993), The biogeochemistry of manganese and iron reduction in marine sediments, *Earth-Science*
890 *Reviews*, *35*(3), 249–284.

891 Burdige, D. J. (2005), Burial of terrestrial organic matter in marine sediments: A re-assessment, *Global*
892 *Biogeochemical Cycles*, *19*(4).

893 Cai, W.-J. (2011), Estuarine and coastal ocean carbon paradox: CO2 sinks or sites of terrestrial carbon incineration?,
894 *Annual review of marine science*, *3*, 123–145.

895 Canfield, D. E., R. Raiswell, and S. H. Bottrell (1992), The reactivity of sedimentary iron minerals toward sulfide,
896 *American Journal of Science*, *292*(9), 659–683.

897 Carter, R., P. Larcombe, J. Dye, M. Gagan, and D. Johnson (2009), Long-shelf sediment transport and storm-bed
898 formation by cyclone winifred, central great barrier reef, australia, *Marine Geology*, *267*(3-4), 101–113.

899 Cathalot, C., C. Rabouille, L. Pastor, B. Deflandre, E. Viollier, R. Buscail, A. Grémare, C. Treignier, and A. Pruski
900 (2010), Temporal variability of carbon recycling in coastal sediments influenced by rivers: Assessing the impact of
901 flood inputs in the Rhône River prodelta, *Biogeosciences*, *7*(3), 1187–1205, doi:10.5194/bg-7-1187-2010. [online]
902 Available from: https://bg.copernicus.org/articles/7/1187/2010/ (Accessed 20 July 2021)

903 Cathalot, C. et al. (2013), The fate of river organic carbon in coastal areas: A study in the rhône river delta using
904 multiple isotopic (δ13C, Δ14C) and organic tracers, *Geochimica et Cosmochimica Acta*, *118*, 33–55.

905 Chakrapani, G. J. (2005), Factors controlling variations in river sediment loads, *Current science*, 569–575.

906 Charmasson, S., O. Radakovitch, M. Arnaud, P. Bouisset, and A.-S. Pruchon (1998), Long-core profiles of 137 cs,
907 134 cs, 60 co and 210 pb in sediment near the rhone river (northwestern mediterranean sea), *Estuaries*, *21*, 367–
908 378.

909 Cheng, P., M. Li, and Y. Li (2013), Generation of an estuarine sediment plume by a tropical storm, *Journal of*
910 *Geophysical Research: Oceans*, *118*(2), 856–868.

911 Copard, Y., F. Eyrolle, O. Radakovitch, A. Poirel, P. Raimbault, S. Gairoard, and C. Di-Giovanni (2018), Badlands as
912 a hot spot of petrogenic contribution to riverine particulate organic carbon to the Gulf of Lion (NW Mediterranean
913 Sea), *Earth Surface Processes and Landforms*, *43*(12), 2495–2509, doi:10.1002/esp.4409. [online] Available from:
914 http://dx.doi.org/10.1002/esp.4409

915 Dai, M. et al. (2022), Carbon fluxes in the coastal ocean: Synthesis, boundary processes, and future trends, *Annual*
916 *Review of Earth and Planetary Sciences*, *50*, 593–626.

917 Dale, A. W., P. Regnier, and P. Van Cappellen (2006), Bioenergetic controls on anaerobic oxidation of methane
918 (AOM) in coastal marine sediments: A theoretical analysis, *American Journal of Science*, *306*(4), 246–294.

919 Dale, A. W., L. Nickelsen, F. Scholz, C. Hensen, A. Oschlies, and K. Wallmann (2015), A revised global estimate of
920 dissolved iron fluxes from marine sediments, *Global Biogeochemical Cycles*, *29*(5), 691–707.

Deflandre, B., A. Mucci, J.-P. Gagné, C. Guignard, and B. jørn Sundby (2002), Early diagenetic processes in coastal marine sediments disturbed by a catastrophic sedimentation event, *Geochimica et Cosmochimica Acta*, *66*(14), 2547–2558.

Eyrolle, F., O. Radakovitch, P. Raimbault, S. Charmasson, C. Antonelli, E. Ferrand, D. Aubert, G. Raccasi, S. Jacquet, and R. Gurriaran (2012), Consequences of hydrological events on the delivery of suspended sediment and associated radionuclides from the Rhône River to the Mediterranean Sea, *Journal of Soils and Sediments*, *12*(9), 1479–1495, doi:10.1007/s11368-012-0575-0. [online] Available from: http://link.springer.com/10.1007/s11368-012-0575-0 (Accessed 2 August 2021)

Ferreira, E., S. Nmor, E. Viollier, B. Lansard, B. Bombled, E. Regnier, G. Monvoisin, C. Grenz, P. Van Beek, and C. Rabouille (2023), Characterization of the benthic biogeochemical dynamics after flood events in the rhône river prodelta: A data-model approach, *Biogeosciences Discussions*, *2023*, 1–27.

Froelich, P. N. (1988), Kinetic control of dissolved phosphate in natural rivers and estuaries: A primer on the phosphate buffer mechanism 1, *Limnology and oceanography*, *33*(4part2), 649–668.

Haese, R., R (2000), The reactivity of iron, in marine geochemistry, in *Marine geochemistry*, edited by H. D. Schulz, pp. 233–261, Springer.

Jørgensen, B. B., A. J. Findlay, and A. Pellerin (2019), The biogeochemical sulfur cycle of marine sediments, *Frontiers in microbiology*, *10*, 849.

Lansard, B., C. Rabouille, L. Denis, and C. Grenz (2008), In situ oxygen uptake rates by coastal sediments under the influence of the Rhône River (NW Mediterranean Sea), *Continental Shelf Research*, *28*(12), 1501–1510, doi:10.1016/j.csr.2007.10.010. [online] Available from: https://linkinghub.elsevier.com/retrieve/pii/S0278434308000769 (Accessed 16 August 2021)

Lansard, B., C. Rabouille, L. Denis, and C. Grenz (2009), Benthic remineralization at the land–ocean interface: A case study of the Rhône River (NW Mediterranean Sea), *Estuarine, Coastal and Shelf Science*, *81*(4), 544–554, doi:10.1016/j.ecss.2008.11.025. [online] Available from: https://linkinghub.elsevier.com/retrieve/pii/S0272771408004599 (Accessed 20 July 2021)

LaRowe, D. E. et al. (2020), The fate of organic carbon in marine sediments-new insights from recent data and analysis, *Earth-Science Reviews*, *204*, 103146.

Mackenzie, F., A. Lerman, and A. Andersson (2004), Past and present of sediment and carbon biogeochemical cycling models, *Biogeosciences*, *1*(1), 11–32.

Maillet, G. M., C. Vella, S. Berné, P. L. Friend, C. L. Amos, T. J. Fleury, and A. Normand (2006), Morphological changes and sedimentary processes induced by the december 2003 flood event at the present mouth of the grand rhône river (southern france), *Marine Geology*, *234*(1-4), 159–177.

Marin, B., and P. Giresse (2001), Particulate manganese and iron in recent sediments of the gulf of lions continental margin (north-western mediterranean sea): Deposition and diagenetic process, *Marine geology*, *172*(1-2), 147–165.

McKee, B. A., R. Aller, M. Allison, T. Bianchi, and G. Kineke (2004), Transport and transformation of dissolved and particulate materials on continental margins influenced by major rivers: Benthic boundary layer and seabed processes, *Continental Shelf Research*, *24*(7-8), 899–926.

Miserocchi, S., L. Langone, and T. Tesi (2007), Content and isotopic composition of organic carbon within a flood layer in the po river prodelta (adriatic sea), *Continental Shelf Research*, *27*(3-4), 338–358.

Montanher, O. C., E. M. L. de M. Novo, and E. E. de Souza Filho (2018), Temporal trend of the suspended sediment transport of the amazon river (1984–2016), *Hydrological sciences journal*, *63*(13-14), 1901–1912.

Moriarty, J. M., C. K. Harris, M. A. Friedrichs, K. Fennel, and K. Xu (2018), Impact of seabed resuspension on oxygen and nitrogen dynamics in the northern gulf of mexico: A numerical modeling study, *Journal of Geophysical Research: Oceans*, *123*(10), 7237–7263.

Moriarty, J. M., M. A. Friedrichs, and C. K. Harris (2021), Seabed resuspension in the chesapeake bay: Implications for biogeochemical cycling and hypoxia, *Estuaries and Coasts*, *44*, 103–122.

967 Morse, J. W., and G. T. Rowe (1999), Benthic biogeochemistry beneath the mississippi river plume, *Estuaries*, *22*(2),
968 206–214.

969 Mucci, A., and H. M. Edenborn (1992), Influence of an organic-poor landslide deposit on the early diagenesis of iron
970 and manganese in a coastal marine sediment, *Geochimica et Cosmochimica Acta*, *56*(11), 3909–3921.

971 Mucci, A., B. Boudreau, and C. Guignard (2003), Diagenetic mobility of trace elements in sediments covered by a
972 flash flood deposit: Mn, fe and as, *Applied geochemistry*, *18*(7), 1011–1026.

973 Nmor, S. I., E. Viollier, L. Pastor, B. Lansard, C. Rabouille, and K. Soetaert (2022), FESDIA (v1. 0): Exploring
974 temporal variations of sediment biogeochemistry under the influence of flood events using numerical modelling,
975 *Geoscientific Model Development*, *15*(19), 7325–7351.

976 Osburn, C. L., J. C. Rudolph, H. W. Paerl, A. G. Hounshell, and B. R. Van Dam (2019), Lingering carbon cycle effects
977 of hurricane matthew in north carolina's coastal waters, *Geophysical Research Letters*, *46*(5), 2654–2661.

978 Palinkas, C., C. Nittrouer, R. Wheatcroft, and L. Langone (2005), The use of 7Be to identify event and seasonal
979 sedimentation near the po river delta, adriatic sea, *Marine Geology*, *222*, 95–112.

980 Pastor, L. et al. (2011a), Influence of the organic matter composition on benthic oxygen demand in the rhône river
981 prodelta (NW mediterranean sea), *Continental Shelf Research*, *31*(9), 1008–1019.

982 Pastor, L., C. Cathalot, B. Deflandre, E. Viollier, K. Soetaert, F. J. R. Meysman, C. Ulses, E. Metzger, and C.
983 Rabouille (2011b), Modeling biogeochemical processes in sediments from the Rhône River prodelta area (NW
984 Mediterranean Sea), *Biogeosciences*, *8*(5), 1351–1366, doi:10.5194/bg-8-1351-2011. [online] Available from:
985 https://bg.copernicus.org/articles/8/1351/2011/ (Accessed 7 July 2021)

986 Pastor, L., C. Rabouille, E. Metzger, A. Thibault de Chanvalon, E. Viollier, and B. Deflandre (2018), Transient early
987 diagenetic processes in Rhône prodelta sediments revealed in contrasting flood events, *Continental Shelf Research*,
988 *166*, 65–76, doi:10.1016/j.csr.2018.07.005. [online] Available from:
989 https://linkinghub.elsevier.com/retrieve/pii/S0278434318300281 (Accessed 7 July 2021)

990 Pont, D., J.-P. Simonnet, and A.-V. Walter (2002), Medium-term changes in suspended sediment delivery to the
991 ocean: Consequences of catchment heterogeneity and river management (rhône river, france), *Estuarine, Coastal*
992 *and Shelf Science*, *54*(1), 1–18.

993 Pont, D., J. W. Day, and C. Ibáñez (2017), The impact of two large floods (1993–1994) on sediment deposition in the
994 Rhône delta: Implications for sustainable management, *Science of The Total Environment*, *609*, 251–262,
995 doi:10.1016/j.scitotenv.2017.07.155. [online] Available from:
996 https://linkinghub.elsevier.com/retrieve/pii/S0048969717318582 (Accessed 2 August 2021)

997 Poulton, S., and R. Raiswell (2002), The low-temperature geochemical cycle of iron: From continental fluxes to
998 marine sediment deposition, *American journal of science*, *302*(9), 774–805.

999 Poulton, S. W., M. D. Krom, and R. Raiswell (2004), A revised scheme for the reactivity of iron (oxyhydr) oxide
1000 minerals towards dissolved sulfide, *Geochimica et cosmochimica acta*, *68*(18), 3703–3715.

1001 Pruski, A. M., R. Buscail, S. Bourgeois, G. Vétion, J. Coston-Guarini, and C. Rabouille (2015), Biogeochemistry of
1002 fatty acids in a river-dominated mediterranean ecosystem (rhône river prodelta, gulf of lions, france): Origins and
1003 diagenesis, *Organic Geochemistry*, *83*, 227–240.

1004 Rabouille, C., and J.-F. Gaillard (1991), Towards the EDGE: Early diagenetic global explanation. A model depicting
1005 the early diagenesis of organic matter, O2, NO3, mn, and PO4, *Geochimica et Cosmochimica Acta*, *55*(9), 2511–
1006 2525.

1007 Rabouille, C. et al. (2021), Early diagenesis in the hypoxic and acidified zone of the northern gulf of mexico: Is
1008 organic matter recycling in sediments disconnected from the water column?, *Frontiers in Marine Science*, *8*, 604330.

1009 Radakovitch, O., V. Roussiez, P. Ollivier, W. Ludwig, C. Grenz, and J.-L. Probst (2008), Input of particulate heavy
1010 metals from rivers and associated sedimentary deposits on the gulf of lion continental shelf, *Estuarine, Coastal and*
1011 *Shelf Science*, *77*(2), 285–295.

1012 Raiswell, R., and D. E. Canfield (1998), Sources of iron for pyrite formation in marine sediments, *American Journal of*
1013 *Science*, *298*(3), 219–245.

1014 Rassmann, J., E. M. Eitel, B. Lansard, C. Cathalot, C. Brandily, M. Taillefert, and C. Rabouille (2020), Benthic
1015 alkalinity and dissolved inorganic carbon fluxes in the Rhône River prodelta generated by decoupled aerobic and
1016 anaerobic processes, *Biogeosciences*, *17*(1), 13–33, doi:10.5194/bg-17-13-2020. [online] Available from:
1017 https://bg.copernicus.org/articles/17/13/2020/ (Accessed 20 July 2021)

1018 Reed, D. C., C. P. Slomp, and B. G. Gustafsson (2011), Sedimentary phosphorus dynamics and the evolution of
1019 bottom-water hypoxia: A coupled benthic–pelagic model of a coastal system, *Limnology and Oceanography*, *56*(3),
1020 1075–1092.

1021 Regnier, P., L. Resplandy, R. G. Najjar, and P. Ciais (2022), The land-to-ocean loops of the global carbon cycle,
1022 *Nature*, *603*(7901), 401–410.

1023 Rickard, D. (1997), Kinetics of pyrite formation by the H2S oxidation of iron (II) monosulfide in aqueous solutions
1024 between 25 and 125 c: The rate equation, *Geochimica et Cosmochimica Acta*, *61*(1), 115–134.

1025 Rickard, D. (2006), The solubility of FeS, *Geochimica et Cosmochimica Acta*, *70*(23), 5779–5789.

1026 Romans, B. W., S. Castelltort, J. A. Covault, A. Fildani, and J. Walsh (2016), Environmental signal propagation in
1027 sedimentary systems across timescales, *Earth-Science Reviews*, *153*, 7–29.

1028 Roussiez, V., W. Ludwig, O. Radakovitch, J.-L. Probst, A. Monaco, B. Charrière, and R. Buscail (2011), Fate of
1029 metals in coastal sediments of a mediterranean flood-dominated system: An approach based on total and labile
1030 fractions, *Estuarine, Coastal and Shelf Science*, *92*(3), 486–495.

1031 Slomp, C. P., H. P. Mort, T. Jilbert, D. C. Reed, B. G. Gustafsson, and M. Wolthers (2013), Coupled dynamics of iron
1032 and phosphorus in sediments of an oligotrophic coastal basin and the impact of anaerobic oxidation of methane, *PloS*
1033 *one*, *8*(4).

1034 Soetaert, K., and T. Petzoldt (2010), Inverse modelling, sensitivity and monte carlo analysis in r using package FME,
1035 *Journal of statistical software*, *33*, 1–28.

1036 Soetaert, K., P. M. Herman, and J. J. Middelburg (1996), A model of early diagenetic processes from the shelf to
1037 abyssal depths, *Geochim. Cosmochim. Acta*, *60*(6), 1019–1040.

1038 Taylor, K. E. (2001), Summarizing multiple aspects of model performance in a single diagram, *Journal of Geophysical*
1039 *Research: Atmospheres*, *106*(D7), 7183–7192.

1040 Tengberg, A., E. Almroth, and P. Hall (2003), Resuspension and its effects on organic carbon recycling and nutrient
1041 exchange in coastal sediments: In situ measurements using new experimental technology, *Journal of Experimental*
1042 *Marine Biology and Ecology*, *285*, 119–142.

1043 Tesi, T., L. Langone, M. Goñi, R. Wheatcroft, S. Miserocchi, and L. Bertotti (2012), Early diagenesis of recently
1044 deposited organic matter: A 9-yr time-series study of a flood deposit, *Geochimica et Cosmochimica Acta*, *83*, 19–36.

1045 Tesi, T., S. Miserocchi, F. Acri, L. Langone, A. Boldrin, J. Hatten, and S. Albertazzi (2013), Flood-driven transport of
1046 sediment, particulate organic matter, and nutrients from the po river watershed to the mediterranean sea, *Journal of*
1047 *Hydrology*, *498*, 144–152.

1048 Tockner, K., and J. A. Stanford (2002), Riverine flood plains: Present state and future trends, *Environmental*
1049 *conservation*, *29*(3), 308–330.

1050 Toussaint, F. et al. (2014), A new device to follow temporal variations of oxygen demand in deltaic sediments: The
1051 LSCE benthic station, *Limnology and oceanography: Methods*, *12*(11), 729–741.

1052 Ulses, C., C. Estournel, X. D. De Madron, and A. Palanques (2008), Suspended sediment transport in the gulf of lions
1053 (NW mediterranean): Impact of extreme storms and floods, *Continental shelf research*, *28*(15), 2048–2070.

1054 Van Cappellen, P., and Y. Wang (1996), Cycling of iron and manganese in surface sediments; a general theory for
1055 the coupled transport and reaction of carbon, oxygen, nitrogen, sulfur, iron, and manganese, *American Journal of*
1056 *Science*, *296*(3), 197–243.

1057 Velde, S. J. van de, C. T. Reinhard, A. Ridgwell, and F. J. Meysman (2020), Bistability in the redox chemistry of
1058 sediments and oceans, *Proceedings of the National Academy of Sciences*, *117*(52), 33043–33050.

1059 Velde, S. van de, V. Van Lancker, S. Hidalgo-Martinez, W. M. Berelson, and F. J. R. Meysman (2018), Anthropogenic
1060 disturbance keeps the coastal seafloor biogeochemistry in a transient state, *Scientific Reports*, *8*(1), 5582,
1061 doi:10.1038/s41598-018-23925-y. [online] Available from: http://www.nature.com/articles/s41598-018-23925-y
1062 (Accessed 11 May 2021)

1063 Viollier, E. et al. (2003), Benthic biogeochemistry: State of the art technologies and guidelines for the future of in situ
1064 survey, *Journal of Experimental Marine Biology and Ecology*, *285*, 5–31.

1065 Wang, Y., and P. Van Cappellen (1996), A multicomponent reactive transport model of early diagenesis: Application
1066 to redox cycling in coastal marine sediments, *Geochimica et Cosmochimica Acta*, *60*(16), 2993–3014.

1067 Wijsman, J., P. Herman, J. Middelburg, and K. Soetaert (2002), A model for early diagenetic processes in sediments
1068 of the continental shelf of the black sea, *Estuarine, Coastal and Shelf Science*, *54*(3), 403–421.

1069 Zebracki, M., F. Eyrolle-Boyer, O. Evrard, D. Claval, B. Mourier, S. Gairoard, X. Cagnat, and C. Antonelli (2015),
1070 Tracing the origin of suspended sediment in a large mediterranean river by combining continuous river monitoring
1071 and measurement of artificial and natural radionuclides, *Science of the Total Environment*, *502*, 122–132.

1072 Zhao, M., S. Zhang, L. G. Tarhan, C. T. Reinhard, and N. Planavsky (2020), The role of calcium in regulating marine
1073 phosphorus burial and atmospheric oxygenation, *Nature communications*, *11*(1), 1–8.